1 **Resolving isomeric posttranslational modifications using a nanopore**

2

3 Tobias Ensslen[1], Kumar Sarthak[2], Aleksei Aksimentiev[2] and Jan C. Behrends[1,3]

4 [1]Laboratory for Membrane Physiology and Technology, Department of Physiology, Faculty of Medicine,

5 University of Freiburg, Freiburg, Germany; [2]Center for Biophysics and Quantitative Biology and

6 Department of Physics, University of Illinois at Urbana-Champaign, Urbana, IL 61801, USA, [3]Freiburg

7 Centre for Materials Research, University of Freiburg, Freiburg, Germany.

8

9 **Posttranslational modifications (PTMs) of proteins are crucial for cellular function but pose analytical**

10 **problems, especially in distinguishing chemically identical PTMs at different nearby locations within the**

11 **same protein. Current methods, such as liquid chromatography-tandem mass spectrometry, are**

12 **technically tantamount to *de novo* protein sequencing[1]. Nanopore techniques may provide a more**

13 **efficient solution, but applying the concepts of nanopore DNA strand sequencing to proteins still faces**

14 **fundamental problems[2–4]. Here, we demonstrate the use of an engineered biological nanopore to**

15 **differentiate positional isomers resulting from acetylation or methylation of histone protein H4, an**

16 **important PTM target[5,6]. In contrast to strand sequencing, we differentiate positional isomers by**

17 **recording ionic current modulations resulting from the stochastic entrapment of entire peptides in the**

18 **pore's sensing zone, with all residues simultaneously contributing to the electrical signal. Molecular**

19 **dynamics simulations show that, in this whole-molecule sensing mode, the non-uniform distribution of**

20 **the electric potential within the nanopore makes the added resistance contributed by a PTM dependent**

21 **on its precise location on the peptide. Optimization of the pore's sensitivity in combination with parallel**

22 **recording and automated and standardized protein fragmentation may thus provide a simple, label-**

23 **free, high-throughput analytical platform for identification and quantification of PTMs.**

24

25   Bacterial pore-forming proteins reconstituted in synthetic lipid membranes have been used as electrical

26   molecular sensors in a variety of tasks[7,8]. Sequencing of DNA with biological pores, in particular, has

27   become an established technique[9–11]. Generally, in molecular sensing by nanopores, the modulation of a

28   nanopore's ionic conductance by a single molecule is used to infer that molecule's identity or sequence.

29   Sequencing by nanopores, as currently done, is based on enzymatically controlled threading of a stretched

30   polymer (DNA or RNA) through pores with short dominant constrictions (MspA, CsgG), so that the partial

31   block of the ionic current is determined by a few monomers (bases) only. By contrast, in whole molecule

32   sensing, all segments of a molecule are simultaneously present within the nanopore and contribute to the

33   current block, which enables the use of a nanopore as a single molecule size spectrometer [12–19]. Recently,

34   the pore formed by the protein toxin aerolysin (AeL) of *Aeromonas hydrophila* was used in this way for

35   high-resolution discrimination of oligo-PEGs[20], short oligonucleotides[21] and oligopeptides[22–24].

36   Harnessing of nanopore technology for applications in proteomics has been an active area of research for

37   some time[2,25], including the detection of PTMs[26–29]. Sequencing proteins by nanopore threading, which

38   would in principle allow detection of PTMs in a site-specific manner, is presently in early stages of

39   development, but still faces the lack of processive motors suitable for moving a polypeptide chain through

40   the nanopore and of physical mechanisms for keeping an unevenly charged peptide taut through the

41   nanopore's constriction[3,4,25,30]. Here we show that site-specific detection of histone PTMs is feasible by

42   whole-molecule nanopore sensing of peptide fragments, requiring neither sequential threading nor

43   uniform charge of the analyte. In contrast to recent work using engineered electrostatic interactions to

44   discriminate phosphoserine and phosphothreonine residues[27], our strategy is not limited to charge-

45   conferring modifications and is capable of differentiating true positional isomers. Furthermore, our all-

46   atom molecular dynamics (MD) simulations[31,32] show that the ability to determine the sites of chemically

47   identical modifications originates from an analyte-induced modulation of the nonuniform electric field

48   inside the nanopore, suggesting a universal approach for electrical sensing of molecular shape.
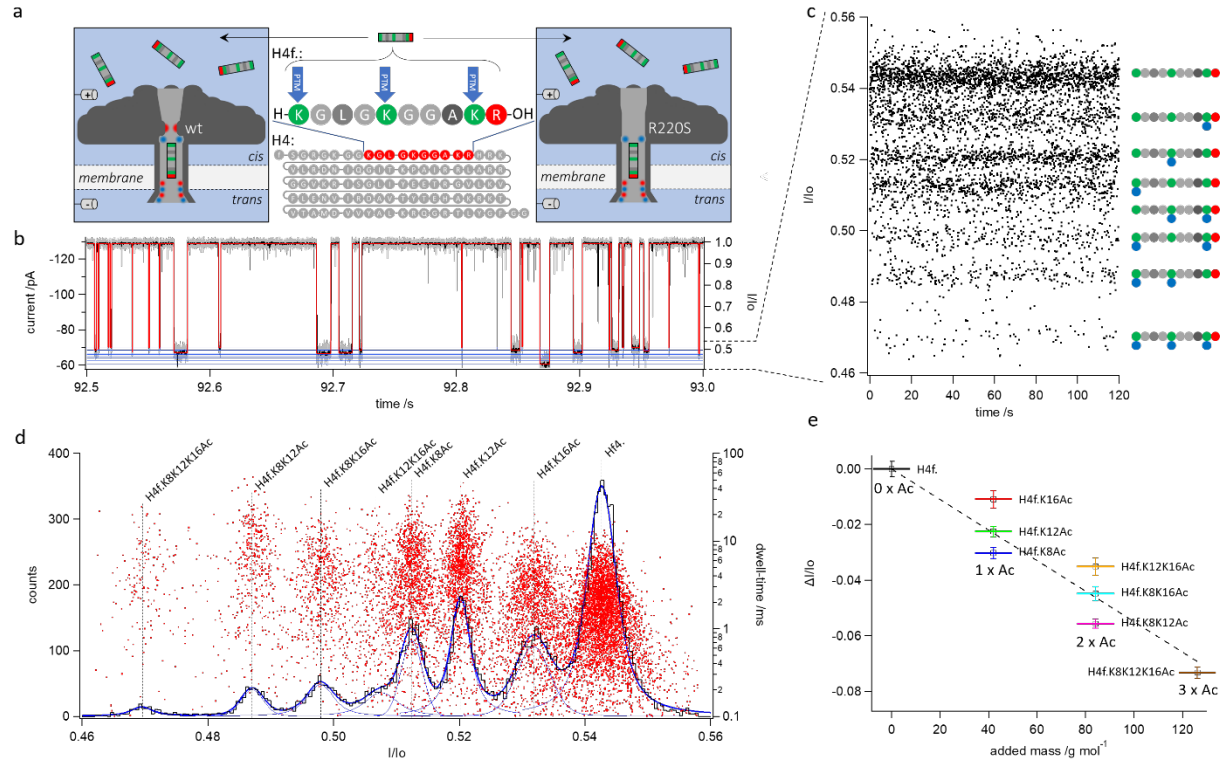
Fig. 1| Discrimination of acetylation-derived positional isomers with the R220S mutant of the aerolysin pore. a, *Experimental set-up and peptide constructs used. Left: schematic representation of the wt-AeL pore reconstituted in a lipid bilayer membrane with the bulky, positively charged arginine in position 220 (R220) as part of the cis-side constriction. Center: Schematic of the full length human H4 protein, and the fragment (H4f.) used in this study. Blue arrows indicate the positions of the three lysins (K8, K12, K16) susceptible to posttranslational modification by acetylation or methylation. Right: the mutant aerolysin pore in which R220 was replaced by a serine, neutralizing the charge and reducing the extent of the constriction. In both representations holder of the pore, a peptide is schematically shown residing in the main beta-barrel, the presumptive sensing region. **b**, Half-a-second current trace of an experiment recorded using the R220S pore in the simultaneous presence of H4f, H4f.K8Ac, H4f.K12Ac, H4f.K16Ac, H4f.K8K12Ac, H4f.K8K16Ac, H4f.K12K16Ac and H4f.K8K12K16Ac and digitally postfiltered at 25 kHz (grey) or 2.5 kHz (black) 3 dB cut-off frequency (see Methods). Red trace indicates the output of the detection algorithm (see methods); blue lines indicate the means of 8 preferred current amplitudes in the blocked state corresponding to the 8 peptoforms. Left y-axis indicates the absolute current (pA), right y-axis shows blocked state current normalized by open pore current (I/Io); **c**: scatterplot of I/Io values against time over 2 min of recording. Note the concentration of data points around 8 distinct levels which can be assigned to the various peptoforms (right) by sequential addition (Extended Data Fig. 2). **d**, Black cityscape: histogram of I/Io levels from the experiment shown in b, c, fitted with the sum (thick blue line) of 8 Voigt peaks [31] (thin blue lines) corresponding to each probability maximum. Red dots: superimposed scatterplot of resistive pulse dwell-time vs. I/Io value. **e**, Shift of maxima in d with respect to the unmodified H4f.-peptide (black) plotted against mass added by acetylations. Error bars give full width at half maximum of Voigt peaks. Note that despite a linear overall dependence of I/Io on mass, the maxima corresponding to peptoforms of identical mass are clearly separated.*

For our proof-of-principle experiments, we chose a decapeptide sequence occurring near the N-terminus of histone protein 4, H4 (K8-R17) (**Fig. 1**a). This protein fragment, H4f., contains three lysine residues (K8, K12, K16) at which acetylation has important functional consequences for gene expression[32,33]. We chose the sequence to include, in particular, lysine K16, as its acetylation was recently found to be important for human development[34], as well as to be an intergenerational gene activation signal in Drosophila[35]. We chose the sequence to be shorter than the common N-terminal tryptic fragment H4(G4-R17) to be

75   commensurate with the length of peptides known to provide good size resolution with the aerolysin

76   pore[22,23].

77   A major consideration for whole-molecule sensing is the dwell-time of the analyte in the nanopore. In the

78   presence of noise, longer current blocks give more precise estimation of the relative residual current and

79   thereby, enhance resolution of subtle differences between analyte molecules[8,20,23] and site-directed

80   mutagenesis of presumptive pore-lining residues can be used to prolong analyte interaction with biological

81   nanopores[28,36–38]. On the other hand, measurement error decreases only with the square root of dwell-

82   times and saturation of the pore may become an issue. In exploratory experiments using arginine-based

83   peptides, we identified a novel functional aerolysin mutant, R220S, in which the dwell-times are

84   approximately doubled with respect to the wild-type and which enhanced differentiation of peptides

85   containing single amino acid substitutions (**Extended Data Fig. 1**). We, therefore, used the R220S mutant

86   for the task of differentiating positional peptide isomers.

87   **Fig. 1** reports results from a typical recording using the R220S aerolysin mutant in the presence of all seven

88   peptide variants (peptoforms), resulting from acetylation of either one, two or all three lysine residues K8,

89   K12 and/or K16 (H4f.K8Ac, H4f.K12Ac, H4f.K16Ac, H4f.K8K12Ac, H4f.K8K16Ac, H4f.K12K16Ac and

90   H4f.K8K12K16Ac), as well as the unmodified fragment Hf4. As shown in **Fig. 1**b, the open pore current of

91   approximately -130 pA at a driving force of -60 mV is, at irregular intervals, interrupted by blocks that reach

92   various, reduced current levels which are situated around 50 % of the open pore current Io (right axis:

93   relative residual current I/Io≅0.5). A plot of the computed event-averaged mean current values of these

94   blocks vs. time (**Fig. 1**c) reveals them to be concentrated at eight preferred relative residual current values.

95   A histogram showing the corresponding probability maxima is shown in **Fig. 1**d. These levels were

96   unequivocally assigned to each species by sequential addition of the peptoforms (see **Extended Data Fig.**

97   **2**). Surprisingly, as also shown by the multi-Voigt peak fits[31] in **Fig. 1**d and **Extended Data Fig. 2**, there is

98   good to excellent separation between the maxima corresponding to the positional isomers for single

99   acetylation (H4f.K16Ac, H4f.K12Ac, H4f.K8Ac) and double acetylation (H4f.K12K16Ac, H4f.K8K16Ac,

100   H4f.K8K12Ac). As expected, the sequence of I/Io-values follows mass, or more likely global volume[8,23], so

101   that increased overall acetylation induces a shift towards deeper blocks. Indeed, a plot of the shift of the

102   mean relative residual current value (ΔI/Io) with respect to unmodified H4f. vs. the mass added by

103   acetylation shows an overall linear relationship (**Fig. 1**e). However, the peptoforms of equal mass

104   (positional isomers) are well separated from each other (**Fig. 1**e), with acetylations towards the N-terminus

105   providing deeper blocks (**Extended Data Fig. 3**a, b). Note the reduction of peak area with increased

106   acetylation due to neutralization of the positive charges of the lysines and the resulting weakening of

107   electrophoretic force on the analyte (Extended Data Fig. 3c).

108   The clear separation between the population maxima is mainly possible because all peptoforms induce

109   blocks with characteristic dwell-times well above 1 ms in the R220S variant (see scatterplot in **Fig. 1**d and

110   **Extended Data Fig. 3**d and **Extended Data Fig. 4**), with acetylation propitiously increasing these values,

111   thus allowing efficient reduction in measurement error by digital averaging for all species. This contrasts

112   with the wild type aerolysin pore, where acetylation induces a strong reduction in dwell-times to well

113   below 1 ms (Extended Data Fig. 5 - **Extended Data Fig. 8**). As evidenced by sequential addition

114   experiments, the different peptoforms block the ionic current to unique levels also in the wild-type pore,

115   and also in the same sequence. However, the measurement error due to shorter dwell-times produces

116   considerable overlap between the I/Io-probability maxima for peptoforms of equal mass (Extended Data

117   Fig. 6, Extended Data Fig. 8a, b).

118   In essence, our findings show that, in both wild type and mutant pores, chemical modifications of residues

119   affect the residual current in a manner dependent on the position of the modification in the peptide chain.

120   This result opens a range of new possibilities for the use of nanopores in probing the structure of single

121   molecules and would not be predicted in the framework of the constant field assumption for ion

122   transport[39].

123   To determine the molecular mechanism enabling the site-selective differentiation of PTMs, we used the

124   steered MD (SMD) protocol[40,41] to pull an H4f.K8Ac peptide through the transmembrane pore of the

125   aerolysin variant R220S (**Fig. 2**a). The sequence of microscopic conformations generated by the SMD run

126   was analyzed using the steric exclusion model (SEM)[42] to determine the relative residual current (I/Io) as

127   a function of the peptide's location within the pore, **Fig. 2**b. The residual current has its highest value close

128   to 1.0 as the peptide enters the pore from the *cis*-side and the lowest value of 0.1 as it passes through the

129   *trans*-side constriction of aerolysin. Starting from the ensemble of conformations generated by pulling the

130   H4f.K8Ac peptide, we obtained conformational ensembles for H4f., singly (H4f.K8Ac, H4f.K12Ac,

131   H4f.K16Ac), doubly (H4f.K8K12Ac, H4f.K8K16Ac, H4f.K12K16Ac) and triply (H4f.K8K12K16Ac) acetylated

132   peptides by computationally mutating the side chains of the respective acetylated residues[23]. Repeating

133   the SEM calculations for the modified peptides produced seven additional profiles of the relative residual

134   current, **Fig. 2**b, all of which appear to be nearly indistinguishable from that of H4f.K8Ac, except in certain

135   regions of the pore. The average simulated residual current of all eight peptides, **Fig. 2**c, was found to be

136   in good agreement with the experimental values when the currents were averaged over the complete

137   sensing volume of wt-AeL[23], or over the region where the deviations were observed (**Extended Data Fig.**

138   **9**). From repeated SMD simulations we learned, however, that the sequence of blockade level's ordering

139   does depend on the global conformation of the peptides, in particular on the global orientation of the

140   peptide with respect to the nanopore (see **Extended Data Fig. 10** and **Extended Data Fig. 11**).

141   Having established a computational model that reproduces experimentally measured differences in the

142   blockade current, we identified the molecular mechanism that enables site-specific determination of

143   PTMs. Whereas a current difference produced by either acetylation or deacetylation is expected, as such

144   a modification changes the overall volume excluded by the peptide from the conductive volume of the

145   nanopore, the transfer of the same modification from one site to another does not alter the excluded

146   volume and thus any effect on pore conductance requires a more detailed examination. To this end, we

147   compared the local density of transmembrane ionic current (the current's z component) in the nanopore

148   blocked by either H4f.K8Ac or H4f.K16Ac peptides, which molecular configurations differ only by the site

149   of acetylation, **Fig. 2**d (see Extended Data Fig. 12 for similar analysis of another peptide conformation from

150   the same MD trajectory). The local current density map, **Fig. 2**e, shows low currents in the regions occupied

151   by the N-terminus of the peptide (i.e., around z=22 Å, residue 8 and 9) and high currents in the parts of

152   the nanopore devoid of the peptide atoms (i.e., around z=6 Å, residues 15-17). The electrostatic potential

153   profile computed for the two peptide conformations, **Fig. 2**f, reveals that the sharpest drop of the potential

154   occurs in the vicinity of residue K8, and that acetylation of that residue considerably increases resistance

155   of the adjacent nanopore volume (**Fig. 2**f, dashed lines). In contrast, acetylation of residue K16 introduces

156   negligible changes to the local nanopore resistance. This is in line with the experimental finding which

157   shows a deepening of the block of the pore as the lysines towards the N-terminus of the peptide are

158   acetylated (Extended Data Fig. 3b). Thus, our analysis points to a microscopic mechanism where a

159   peptide's confinement within the nanopore creates a conductive volume of a highly non-uniform shape.

160   Because of this non-uniform shape, a local change of the volume's cross section due to a PTM can alter

161   the overall conductance of the nanopore by an amount that depends on the location of the PTM within

162   the conductive volume, similar to an effect produced by placing a boulder in either rapids or a backwater

163   section of a mountain stream, **Fig. 2**g.

164
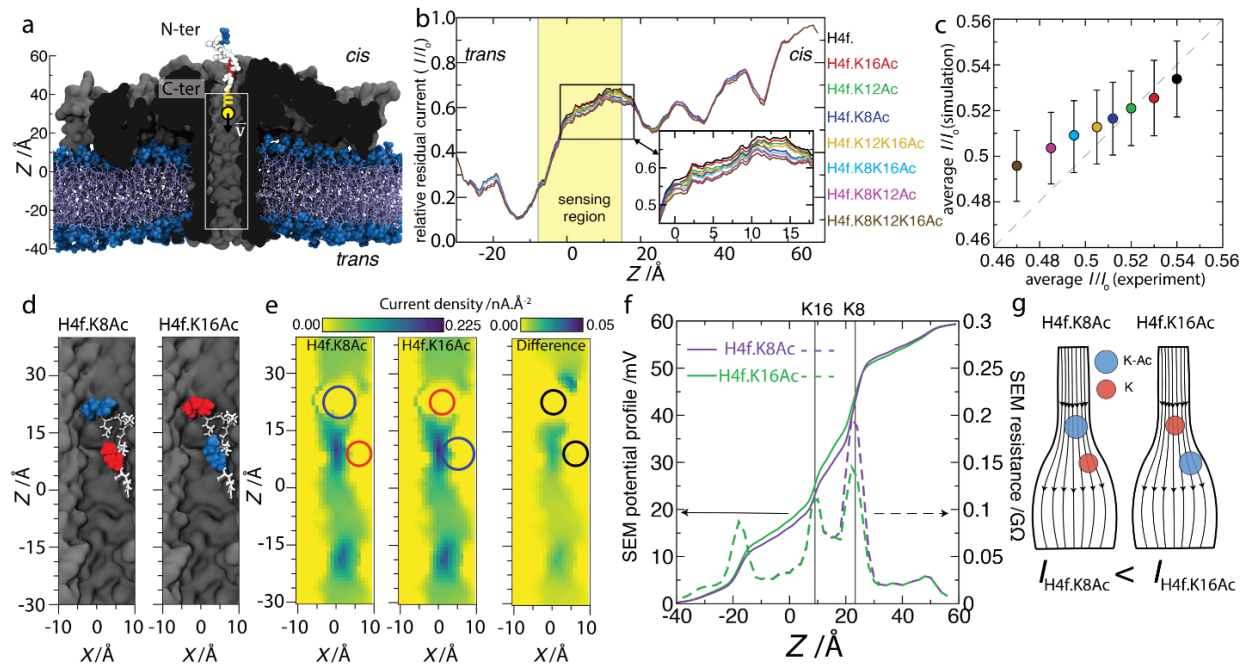
Fig. 2| Microscopic mechanism of site-selective PTM detection. a, *Initial state of a 100 ns steered MD simulation where an*
H4f.K8Ac peptide (vdw spheres) is pulled by a harmonic spring with a constant velocity of 1 Å/ns through an aerolysin nanopore
(cutaway molecular surface), embedded in a lipid membrane (blue) and submerged in 2 M KCl electrolyte (not shown). The C-
terminus of the peptide is oriented towards the trans-side of the membrane. The white rectangle indicates the location of the
nanopore volume shown in panels d and e. **b,** *Relative residual current versus center of mass z coordinate of the acetylated H4f.*
peptides. The coordinate axis is defined in panel a. The currents were computed using SEM[42] and running-averaged with a 5 Å
window. The highlighted region shows the sensing volume (-9 Å < z < 15 Å) of the wt-AeL pore[23]. The inset shows a zoomed-in view
of the main plot. **c,** *Simulated vs. experimental average relative currents produced by the acetylated peptides within the sensing*
region of aerolysin. Colors represent peptide variants as defined in panel b. The error bars show the standard error calculated using
100 current values from the sensing region of the nanopore. **d,** *Representative conformation of the H4f.K8Ac peptide in the sensing*
region of the nanopore and the corresponding computational model of the H4f.K16Ac peptide. The peptide residues are drawn as
white sticks except residues K8 and K16, which are shown as vdW spheres colored according to their acetylation state: acetylated
(blue) and unmodified (red). **e,** *local density of transmembrane ion current (its z component) near the H4f.K8Ac (left) and H4f.K16Ac*
(center) peptides and their difference (H4f.K16Ac-H4f.K8Ac, right). The currents were computed using SEM over a 1 Å grid. The
heat map shows a cross section of the nanopore volume along the pore axis. The circles indicate the approximate locations of the
K8 and K16 residues. **f,** *Electrostatic potential along the nanopore axis for the H4f.K8Ac (purple) and H4f.K16Ac (green) peptide*
systems (solid lines, left axis) and local resistance of the nanopore volume (dashed lines, right axis). The local resistance was
computed from the local electrostatic potential using 4 Å segments. **g,** *Schematics illustrating the microscopic mechanism enabling*
site-specific PTM detection via a blockade current measurement. The blue and red balls represent acetylated and unmodified lysine
residues, respectively.

To determine whether our result can, in principle, be generalized to other PTMs of histone proteins, we
attempted to analyze site-selective mono- and trimethylation of lysines K8, K12 and K16 using the R220S
mutant aerolysin pore. In order to allow direct comparison with the acetylation results, we used the same
H4f. as above, despite the fact that K20, rather than K8, K12 and K16, is reported to be a known H4
methylation target[43,44].

7

191   As shown in **Fig. 3**a, clearly different maxima were apparent in the relative residual current (I/Io) histogram

192   for nonmethylated and singly, doubly and triply monomethylated forms of H4f. As in the case of

193   acetylation, successive monomethylation at one, two or three residues resulted in a progressive shift of

194   the I/Io-maxima towards deeper blocked levels that was linearly related to added mass (**Fig. 3**d). In keeping

195   within the smaller added mass of methylation (14 g/mol) vs. acetylation (42 g/mol), the total shift by triple

196   monomethylation was less than that by triple acetylation; however, the steepness of the relationship

197   between the shift of ΔI/Io and the added mass was higher for methylation than for acetylation. While the

198   histogram in **Fig. 3**a shows no obvious separation between the maxima for the positional isomers

199   H4f.K8me, H4f.K12me, H4f.K16me or H4f.K8K12me, H4f.K8K16me, H4f.K12K16me, it became evident in

200   sequential addition experiments that each species contributed a population of resistive pulses with a

201   characteristic mean relative current I/Io.

202   As shown in **Fig. 3**b, equimolar addition of H4f.K12me to the *cis*-compartment already containing

203   H4f.K8me not only made the blockade events more frequent, but also broadened the I/Io-distribution and

204   shifted its maximum towards a smaller value. A similar trend was observed when H4f.K16me was added

205   to a *cis*-compartment containing H4f.K8me and H4f.K12me. In both cases, this shift and broadening could

206   be accounted for by the contribution of an additional population, characterized by a slightly shifted mean,

207   as shown by the Voigt fits in **Fig. 3**b and **Extended Data Fig. 15**a-c. Different population maxima could also

208   be determined by sequential addition of H4f.K8K12me, H4f.K8K16me and H4f.K12K16me (**Fig. 3**c and

209   **Extended Data Fig. 15**d-f).

210   We note that, while not allowing for single-passage identification, as for acetylation, the site-specific

211   sensitivity of the mutant pore for monomethylation is sufficient to allow for a quantitative analysis of

212   methylated peptoforms, as shown above, given appropriate calibration of on-rates to correct for the loss

213   of electrophoretic susceptibility.

214   The study of lysine trimethylation of H4f. suggests that relative abundance of isomer populations can not

215   only be discerned from the blockade levels (I/Io) but also from the analysis of the dwell-time distributions.

216   The positional isomers H4f.K8me$_3$ and H4f.K12me$_3$ could not be *prima facie* distinguished on the basis of

217   the I/Io-distributions in the presence of all seven species but H4f.K16me$_3$ showed a clearly distinct

218   maximum that was shifted towards lower residual currents. Conversely, the maxima for doubly

219   trimethylated H4f.K8K12me$_3$ and H4f.K12K16me$_3$ were lumped together in one peak, while H4f.K8K16me$_3$

220   produced a distinct peak, shifted towards higher residual current levels (**Fig. 3**, **Extended Data Fig. 16**). As

221   before, closer analysis of sequential addition experiments revealed a small shift in the population mean

222   upon adding H4f.K12me$_3$ to H4f.K8me$_3$ or H4f.K12K16me$_3$ to H4f.K8K12me$_3$, which enabled the use of the

223   fitting procedure previously shown for monomethylation to extract separate I/Io values for the two

224   overlapping species (**Fig. 3**f, g and **Extended Data Fig. 18**). Furthermore, by addition of H4f.K12me$_3$ to

225   H4f.K8me$_3$ or H4f.K12K16me$_3$ to H4f.K8K12me$_3$ the monoexponential distribution of event dwell-times

226   contained in the maximum (τ≈2 and 5 ms, respectively) was converted into a double-exponential

227   distribution due to the appearance of a second exponential population with longer dwell-times (τ'≈5 and

228   10 ms, respectively, **Fig. 3**f, g inset and **Extended Data Fig. 17**). The relative weights of the two exponential

229   components may, therefore, also be used to estimate the relative abundance of these isomeric

230   peptoforms following appropriate correction for on-rates. Again, we found an overall linear relationship

231   between the shift in I/Io, added mass and the steepness for the relation for trimethylation was

232   indistinguishable from that for acetylation. Synthesis of triply trimethylated H4f. was attempted at two

233   commercial sources, but failed.

234
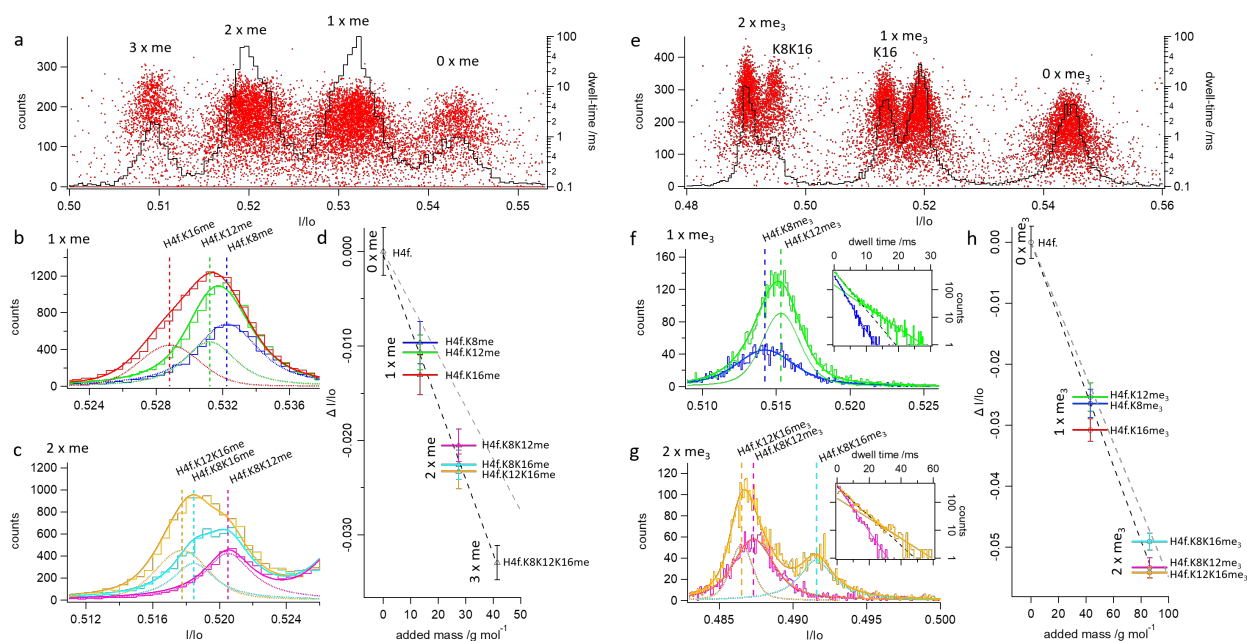
*Fig. 3| Discrimination of positional isomers from mono- and trimethylation with the R220S mutant. a, Histogram of I/Io-values (black) and scatterplot of dwell-time vs. I/Io (red) in the presence of all singly, doubly and triply monomethylated species, as well as of unmodified H4f. Unlike for acetylation, the positional isomers (singly monomethylated H4f.K8me, H4f.K12me and H4f.K16me, as well as doubly monomethylated H4f.K8K12me, H4f.K8K16me and H4f.K12K16me) are not obviously separated in terms of blockade levels, as their maxima overlap (for assignment of peaks by sequential addition see **Extended Data Fig. 13** - **Extended Data Fig. 15**). However, as shown in b and c, sequential addition of isomeric species leads to successive broadening of the maxima, which can be accounted for by the contribution of populations isomeric species with different means. By fitting the I/Io-histograms (cityscapes) with a sum (thick lines) of Voigt peaks (thin lines), the respective position of the maximum of the added peptide can be determined. b, Sequential addition of singly monomethylated species H4f.K8me (blue), after addition of H4f.K12me (green) and after addition of H4f.K16me (red); c: sequential addition of doubly monomethylated species H4f.K8K12me (magenta), after addition of H4f.K8K16me (turquois) and after addition of H4f.K12K16me (gold); For a complete account of the sequential addition experiment see **Extended Data Fig. 15**. d, Shift of maxima with respect to that for unmodified H4f. plotted against the mass added by monomethylation; e: histogram of I/Io-values (black) and scatterplot of dwell-time vs. I/Io (red) in the presence of unmodified*

9

249 *H4f., as well as all singly and doubly trimethylated species. In this case, the maxima for H4f.K8me$_3$ and H4f.K12me$_3$, as well as*
250 *those for H4f.K8K12me$_3$ and H4f.K12K16me$_3$, respectively, overlap in one peak whereas those for H4f.K16me$_3$ and H4f.K8K16me$_3$*
251 *are strongly shifted to deeper (H4f.K16me$_3$) and more shallow blocks (H4f.K8K16me$_3$). For assignment of peaks by sequential*
252 *addition see **Extended Data Fig. 16** - **Extended Data Fig. 18**; **f**: sequential addition of singly trimethylated species H4f.K8me$_3$ (blue)*
253 *and after addition of H4f.K12me$_3$ (green). Note the shift towards longer dwell-times and failure of monoexponential fit (dashed*
254 *line) after addition of H4f.K12me$_3$; **g**, Sequential addition of singly trimethylated species H4f.K8K12me$_3$ (turquois), after addition*
255 *of H4f.K8K16me$_3$ (magenta) and H4f.K12K16me$_3$ (gold). Insets in f and g: dwell-time histograms for the two overlapping species.*
256 *Note the shift to longer dwell-times and departure from monoexponential distribution (dashed lines) upon addition of H4f.K12me$_3$*
257 *or H4f.K12K16me$_3$. **h**, Shift of maxima with respect to that for unmodified H4f. plotted against the mass added by trimethylation;*
258 *All histograms in b, c and f, g were generated from recordings lasting 300 s, making them directly comparable. Grey dashed lines*
259 *in e and h represent the relationship between the shift in I/Io and added mass for acetylation (see **Fig. 1**e).*

260

261 In summary, we have shown that an engineered aerolysin nanopore can be used to quantitatively analyze
262 both acetylation and methylation in a position-sensitive fashion by distinguishing between peptoforms of
263 equal mass on the basis of depth-of-block and, in some cases, duration of resistive pulses. The mechanism
264 of discrimination by resistive current can be explained by the action of a strongly inhomogeneous electric
265 field that is shaped by the pore structure, as well as by the conformation of the confined peptide itself
266 (**Fig. 2**). The dependence on the peptide's conformation also explains for the fact that the sequence of
267 mean I/Io-values for PTM of the different lysines is different for each of the three PTMs analyzed, see
268 **Extended Data Fig. 19**. The higher sensitivity of the mutant pore relative to the wild-type likely originates
269 from a powerful molecular trap that the aerolysin pore provides[23], and which becomes more efficient upon
270 removal of the bulky and positively charged R220 (**Extended Data Fig. 20**, **Extended Data Fig. 21**).
271 Additional mutations of the pore can be envisaged which, in combination with R220S, will lead to further
272 kinetic optimization also for the use with tryptic peptides containing more than ten amino acids. To further
273 increase differentiation among the positional isoforms, future work will focus on reducing instrumental
274 noise[45] and on protein engineering to reducing the conformational degree of freedom of peptides in the
275 pore. Thus, in a combination of parallel high-resolution electrophysiology[15,18] with standardized and
276 automated enzymatic generation of peptide fragments[46], whole molecule sensing with the aerolysin
277 nanopore has the potential of being implemented in a practical technology to rapidly detect PTMs with
278 positional resolution without requiring strand sequencing of proteins.

279

280 **Methods (online only)**

281 **Mutagenesis, Expression and Purification**

282 AeL-R220S single point mutagenesis was carried out following a four primer PCR protocol, followed by

283 standard overlap-PCR. Gene flanking and mutagenesis primers were designed with the sequences depicted

284 below and purchased from Eurofins Genomics GmbH (Ebersberg, Germany).

primer	forward	reverse
flanking	GAA GAC ATG GAT GTG ACC	GCT AGT TAT TGC TCA GCG G
mutation	GTC ACC CTG TCC TAC GAC ACA GCC ACC AAC	TGT GTC GTA GGA CAG GGT GAC GTC ATA GCC

285

286 The mutated insert, as well as the pET22b(+) vector were restricted by BamHI and XhoI (Thermo Fisher

287 Scientific, Waltham, MA, USA) and ligated with T4 DNA Ligase (Fermentas - Thermo Fisher Scientific,

288 Waltham, MA, USA). Mini-scale plasmid preparation was performed after transformation of XL1-Blue

289 competent cells via heat-shock prior to DNA sequencing (Eurofins Genomics GmbH, Ebersberg, Germany).

290 Subsequent max-scale plasmid preparation was performed after transformation of XL1-Blue competent

291 cells with the pET22b(+)::plb::pAeL-R220S-His$_6$ vector via heat-shock. Successful transformation of the

292 cells with vector material containing the insert was verified by enzymatic control restriction using NdeI,

293 XhoI and BamHI (Thermo Fisher Scientific, Waltham, MA, USA) prior to verification of the final plasmid's

294 nucleotide sequence (Eurofins Genomics GmbH, Ebersberg, Germany).

295 Biosynthesis of wt-pAeL and pAeL-R220S was carried out in BL21(DE3)pLysS competent cells after

296 transformation with the corresponding pET22b(+)::plb::pAeL-His$_6$ construct and cultivation at 37 °C. Gene

297 expression was induced at OD600=0.6 by addition of 500 µM IPTG and verified by SDS-PAGE analysis. Cells

298 were further incubated at 18 °C and harvested by centrifugation (1 h, 4400 rpm, 4 °C) when no further

299 change of the OD600 was observed. Cells were washed with cold PBS and pelleted by centrifugation

300 (45 min, 4400 rpm, 4 °C). Cells were disrupted by ultrasonication and debris removed by

301 ultracentrifugation (100'000 xg, 2 h, 4 °C). Protein purification was carried out by Ni-affinity-

302 chromatography (AFI), followed by size-exclusion-chromatography (SE) using an ÄKTA HPLC purifier

303 system (GE Healthcare/Amersham Bioscience, Chalfont St Giles, Great Britain), equipped with a 5 mL

304 HisTrap™HP or a Superdex 200-Increase 10/300 GL column. Protein containing AFI elutions were pooled

305 and concentrated to a final volume of 250 µL, prior to SE using Amicon®Ultra 15 mL centrifuge filters with

306 a molecular weight cutoff of 10 kDa (Merck KGaA, Darmstadt, Germany). Purity of the SE elutions was

307 verified by SDS-PAGE and the protein concentration determined in a Bradford assay (Coomassie brilliant

11

308   blue G-250, BioRad, Hercules, CA, USA). Final protein samples were adjusted to 1 mg/mL, nitrogen shock-

309   frozen and stored at -80 °C. Activation of pAeL was carried out before an experiment by application of

310   trypsin (Promega, Madison, WI, USA) at room-temperature within 15 min.

311

312   **Electrophysiology and data analysis**

313   Nanopore recordings were performed using a modified version of the Orbit16 device (Nanion

314   Technologies, Munich, Germany using MECA 16 microelectrode cavity arrays (Ionera Technologies,

315   Freiburg, Germany) as previously detailed[8,18,23]. Briefly, one of 16 coplanar gold lines leading to MECA 16-

316   cavities (50 μm diam.) was directly contacted with a 1 cm unshielded silver wire to the head-stage of an

317   Axopatch 200B (Molecular Devices, Sunnyvale, CA, USA) patch clamp amplifier operated in capacitive

318   feedback mode at 50 mV/pA gain with the internal low-pass-filter set to 100 kHz cut-off (-3dB). The output

319   signal was passed through an external low-pass Bessel filter (npi electronic, Tamm, Germany, 8 pole,

320   custom version of LHBF-48X-8HL) set to 50 kHz cut-off and digitized at 1 MHz sampling rate using a PCI-

321   6251 16 bit ADC interface (National Instruments, Austin, TX, USA) controlled by GePulse software (Michael

322   Pusch, University of Genoa, Italy). Event-averaged current level detection was performed using

323   thresholding on the differentially rectified signal as shown before[20,23] and explained in detail in Ref[8].

324   Further analysis and graphing were performed using IgorPro8 (Wavemetrics, Portland, OR, USA).

325

326   **Molecular dynamics simulations**

327   **General MD methods:** all MD simulations were carried out using NAMD2[47], a 2 fs integration timestep,

328   periodic boundary conditions, the CHARMM36[48] force field and CUFIX corrections to non-bonded

329   interactions[49]. The covalent bonds containing hydrogen atoms in water were restrained using the SETTLE

330   algorithm[50], and in protein using the RATTLE algorithm[51] Long-range electrostatic interactions were

331   evaluated using the particle mesh Ewald method[52] on a 1 Å grid. Constant pressure was maintained using

332   a Nosé-Hoover Langevin piston[53]. Constant temperature was maintained by coupling the non-hydrogen

333   atoms of the lipid to a Langevin thermostat (Brünger, A. T. X-PLOR: version 3.1: a system for x-ray

334   crystallography and NMR (Yale University Press, 1992)) with a 5 ps^{-1} damping constant. The van der Waals

335   forces were calculated with a switching distance of 10 Å and a cutoff of 12 Å. Local interactions were

336   evaluated every time step and full electrostatics every second time step.

337   **All-atom model of aerolysin:** the all-atom model of the aerolysin-R220S nanopore was built starting from

338   a pre-equilibrated (20 ns), solvated model of wt-AeL embedded in a 1,2-diphytanoyl-sn-glycero-3-

339   phosphocholine (DPhPC) ¬lipid bilayer[23] The R220S mutation was introduced using the psfgen package of

340   VMD[54] The number of K^+ and Cl^- ions was adjusted to produce an electrically neutral system containing

341   2 M KCl solution. Upon assembly, the system underwent 1'000 steps of energy minimization and then

342   equilibrated in the constant number of atoms (430'567), pressure (1 bar) and temperature (293 K)

343   ensemble for 5 ns while restraining the C-α atoms of the protein to their initial coordinates. During the

344   equilibration, the area of the lipid bilayer was kept constant while the system changed its size along the

345   bilayer normal. All subsequent simulations were carried out in a constant number of atoms, volume, and

346   temperature ensemble, where the volume (18.93 nm × 18.93 nm × 11.56 nm) was set to the average value

347   observed within the 5 ns equilibration. The transmembrane bias V=-60 mV was induced by applying a

348   constant electric field, E=-V/Lz, normal to the lipid bilayer, where Lz was the dimension of the system along

349   normal to the bilayer[55] Each C-α atom of aerolysin was harmonically restrained (with a spring constant of

350   69.5 pN/nm) to maintain the same coordinate as in the last frame of the equilibration trajectory.

351   **Simulations of current blockades:** an all-atom model of the H4f. peptide (H-KGLGKGGAKR-OH) was

352   obtained by mutating the side chains of a pre-equilibrated 10-residue peptide taken from a previous

353   study[56]. The N-terminal lysine was acetylated to obtain a microscopic model of the H4f.K8Ac peptide. The

354   peptide was then aligned with the nanopore axis and placed near the *cis*-entrance of the pore such that

355   the C-terminal of the peptide faced the *trans*-side of the pore (**Fig. 2**a). The peptide was then pulled along

356   the pore axis using the SMD method[40,41], while restraining the C-α atoms of aerolysin to their equilibrated

357   coordinates. During the 100 ns SMD run, the center of mass (CoM) of the peptide was coupled to a

358   template particle by means of a harmonic potential (with a spring constant of 4'865 pN/nm) while the

359   templated particle was pulled along the nanopore axis with a constant velocity of 1 Å/ns. The residual

360   current was then calculated using SEM[42] for a set of microscopic configurations taken from the SMD

361   simulation every 0.2 ns, yielding 500 relative residual current values. The currents were sorted in

362   ascending order according to the CoM z coordinate and then averaged using a 5 Å running average

363   window. These averaged currents are plotted in **Fig. 2**b. Using our previously described method [23], each

364   conformation was computationally mutated to obtain microscopic representations of H4f. and all single

365   (H4f.K8Ac, H4f.K12Ac, H4f.K16Ac), double (H4f.K8K12Ac, H4f.K8K16Ac, H4f.K12K16Ac) and triple

366   (H4f.K8K12K16Ac) acetylation peptides. The residual currents for each mutated peptide conformations,

367   **Fig. 2**b, were calculated and averaged using the same protocol.

368

13

380

381 **Author contributions** T.E. and J.C.B. conceived and designed experimental work, T.E. performed

382 electrophysiological experiments, molecular biology and protein purification, T.E. and J.C.B. analysed

383 experimental data, K.S. and A.A. designed MD simulations, K.S. performed MD simulations, K.S. and A.A.

384 analysed MD simulations, T.E. J.C.B. K.S. and A.A prepared figures, T.E., J.C.B. and A.A. wrote the

385 manuscript.

386

387 **Competing interests** J.C.B. is co-founder and shareholder of Nanion Technologies GmbH, Munich,

388 Germany and Ionera Technologies GmbH, Freiburg, Germany

389

390 **Correspondence and requests for materials** should be addressed to A.A. or J.C.B.

391

392   References:

393   1. Leutert, M., Entwisle, S. W. & Villén, J. Decoding post translational modification crosstalk with

394   proteomics. *Mol Cell Proteomics* 20, 100129 (2021).

395   2. Alfaro, J. A. *et al.* The emerging landscape of single-molecule protein sequencing technologies. *Nat*

396   *Methods* 18, 604–617 (2021).

397   3. Yan, S. *et al.* Single Molecule Ratcheting Motion of Peptides in a Mycobacterium smegmatis Porin A

398   (MspA) Nanopore. *Nano Lett* 21, 6703–6710 (2021).

399   4. Brinkerhoff, H., Kang, A. S. W., Liu, J., Aksimentiev, A. & Dekker, C. Multiple rereads of single proteins

400   at single–amino acid resolution using nanopores. *Science* eabl4381 (2021) doi:10.1126/science.abl4381.

401   5. Chen, Q. Y., Costa, M., Sun, H. & USA, D. of E. M., NYU School of Medicine, Tuxedo, NY 10987,.

402   Structure and function of histone acetyltransferase MOF. *Aims Biophysics* 2, 555–569 (2015).

403   6. Bowman, G. D. & Poirier, M. G. Post-Translational Modifications of Histones That Influence

404   Nucleosome Dynamics. *Chem Rev* 115, 2274–2295 (2015).

405   7. Kasianowicz, J. J. *et al.* Analytical applications for pore-forming proteins. *Biochimica Et Biophysica Acta*

406   *Bba - Biomembr* 1858, 593–606 (2016).

407   8. Piguet, F. *et al.* Pore-forming toxins as tools for polymer analytics: From sizing to sequencing. *Methods*

408   *Enzymol* 649, 587–634 (2021).

409   9. Derrington, I. M. *et al.* Nanopore DNA sequencing with MspA. *Proc National Acad Sci* 107, 16060–

410   16065 (2010).

411   10. Laszlo, A. H. *et al.* Decoding long nanopore sequencing reads of natural DNA. *Nat Biotechnol* 32, 829–

412   833 (2014).

413   11. Lin, B., Hui, J. & Mao, H. Nanopore Technology and Its Applications in Gene Sequencing. *Biosensors*

414   11, 214 (2021).

415   12. Robertson, J. W. F. *et al.* Single-molecule mass spectrometry in solution using a solitary nanopore.

416   *Proc National Acad Sci* 104, 8207–8211 (2007).

417   13. Rodrigues, C. G., Machado, D. C., Chevtchenko, S. F. & Krasilnikov, O. V. Mechanism of KCl

418   Enhancement in Detection of Nonionic Polymers by Nanopore Sensors. *Biophys J* 95, 5186–5192 (2008).

419   14. Reiner, J. E., Kasianowicz, J. J., Nablo, B. J. & Robertson, J. W. F. Theory for polymer analysis using

420   nanopore-based single-molecule mass spectrometry. *Proc National Acad Sci* 107, 12080–12085 (2010).

421   15. Baaken, G., Ankri, N., Schuler, A.-K., Rühe, J. & Behrends, J. C. Nanopore-Based Single-Molecule Mass

422   Spectrometry on a Lipid Membrane Microarray. *Acs Nano* 5, 8080–8088 (2011).

15

423   16. Balijepalli, A., Robertson, J. W. F., Reiner, J. E., Kasianowicz, J. J. & Pastor, R. W. Theory of Polymer–
424   Nanopore Interactions Refined Using Molecular Dynamics Simulations. *J Am Chem Soc* 135, 7064–7072
425   (2013).

426   17. Zheng, T., Baaken, G., Vellinger, M., Behrends, J. C. & Rühe, J. Generation of chip based
427   microelectrochemical cell arrays for long-term and high-resolution recording of ionic currents through
428   ion channel proteins. *Sensors Actuators B Chem* 205, 268–275 (2014).

429   18. Martinez, J. M. del R., Zaitseva, E., Petersen, S., Baaken, G. & Behrends, J. C. Automated Formation of
430   Lipid Membrane Microarrays for Ionic Single-Molecule Sensing with Protein Nanopores. *Small* 11, 119–
431   125 (2015).

432   19. Talarimoghari, M., Baaken, G., Hanselmann, R. & Behrends, J. C. Size-dependent interaction of a 3-
433   arm star poly(ethylene glycol) with two biological nanopores. *The European Physical Journal E* 41, 77
434   (2018).

435   20. Baaken, G. *et al.* High-Resolution Size-Discrimination of Single Nonionic Synthetic Polymers with a
436   Highly Charged Biological Nanopore. *Acs Nano* 9, 6443–6449 (2015).

437   21. Cao, C. *et al.* Discrimination of oligonucleotides of different lengths with a wild-type aerolysin
438   nanopore. *Nature Nanotechnology* 11, 713–718 (2016).

439   22. Piguet, F. *et al.* Identification of single amino acid differences in uniformly charged homopolymeric
440   peptides with aerolysin nanopore. *Nat Commun* 9, 966 (2018).

441   23. Ouldali, H. *et al.* Electrical recognition of the twenty proteinogenic amino acids using an aerolysin
442   nanopore. *Nature Biotechnology* 38, 176–181 (2020).

443   24. Howorka, S. & Siwy, Z. S. Reading amino acids in a nanopore. *Nature Biotechnology* 1–2 (2020)
444   doi:10.1038/s41587-019-0401-y.

445   25. Asandei, A. *et al.* Nanopore-Based Protein Sequencing Using Biopores: Current Achievements and
446   Open Challenges. *Small Methods* 4, 1900595 (2020).

447   26. Harrington, L., Alexander, L. T., Knapp, S. & Bayley, H. Single-Molecule Protein Phosphorylation and
448   Dephosphorylation by Nanopore Enzymology. *Acs Nano* 13, 633–641 (2019).

449   27. Li, S. *et al.* T232K/K238Q Aerolysin Nanopore for Mapping Adjacent Phosphorylation Sites of a Single
450   Tau Peptide. *Small Methods* 4, 2000014 (2020).

451   28. Huo, M., Hu, Z., Ying, Y. & Long, Y. Enhanced identification of Tau acetylation and phosphorylation
452   with an engineered aerolysin nanopore. *Proteomics* 2100041 (2021) doi:10.1002/pmic.202100041.

453   29. Zhang, L. *et al.* Detection of single peptide with only one amino acid modification via electronic
454   fingerprinting using reengineered durable channel of Phi29 DNA packaging motor. *Biomaterials* 276,
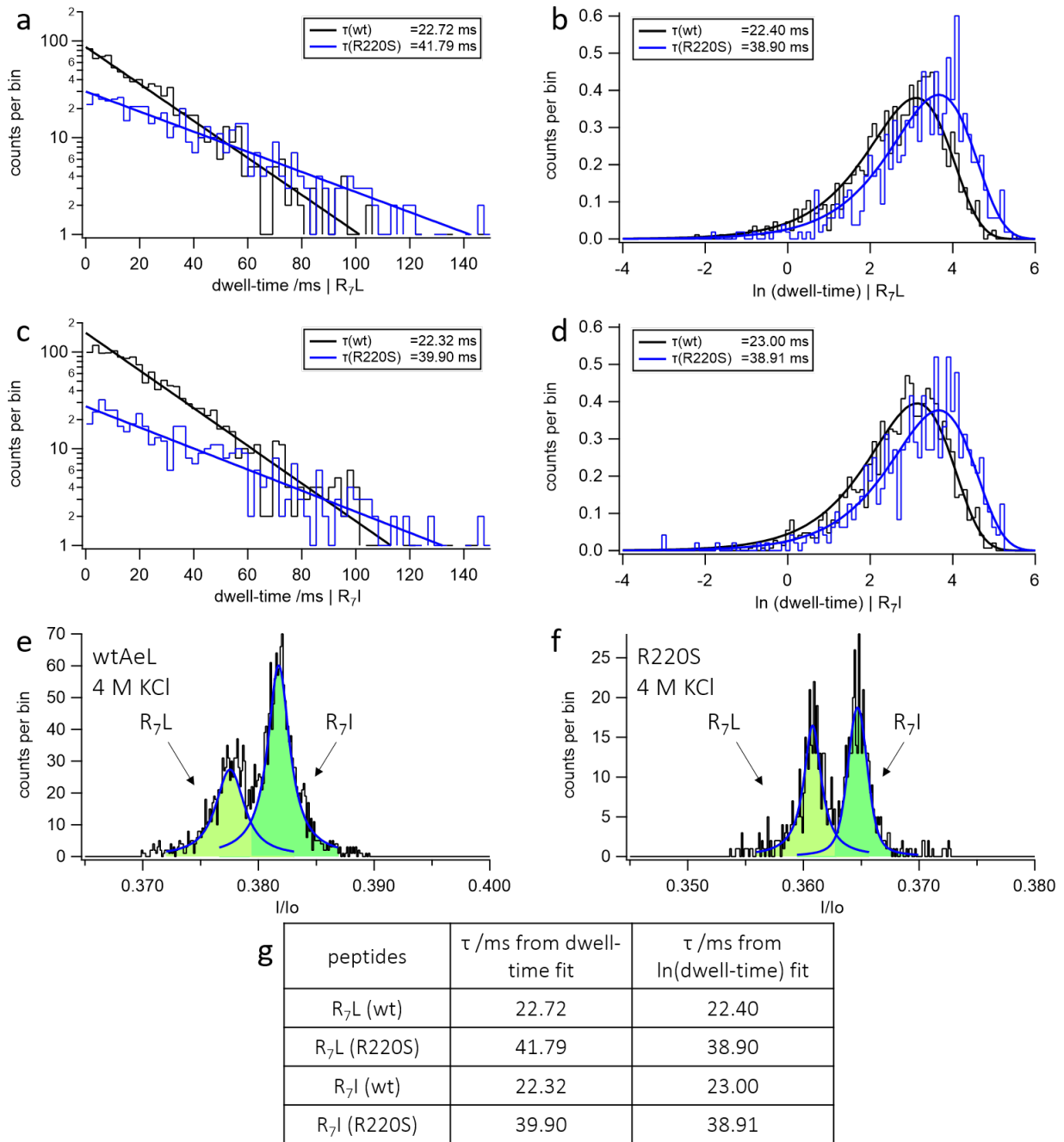455   121022 (2021).

456   30. Rosen, C. B., Rodriguez-Larrea, D. & Bayley, H. Single-molecule site-specific detection of protein
457   phosphorylation with a nanopore. *Nat Biotechnol* 32, 179–181 (2014).

458   31. Reiner, J. E. *et al.* The effects of diffusion on an exonuclease/nanopore-based DNA sequencing
459   engine. *J Chem Phys* 137, 214903 (2012).

460   32. Lang, D. *et al.* Probing the acetylation code of histone H4. *Proteomics* 13, 2989–2997 (2013).

461   33. Shahbazian, M. D. & Grunstein, M. Functions of Site-Specific Histone Acetylation and Deacetylation.
462   *Annu Rev Biochem* 76, 75–100 (2007).

463   34. Basilicata, M. F. *et al.* De novo mutations in MSL3 cause an X-linked syndrome marked by impaired
464   histone H4 lysine 16 acetylation. *Nat Genet* 50, 1442–1451 (2018).

465   35. Samata, M. *et al.* Intergenerationally Maintained Histone H4 Lysine 16 Acetylation Is Instructive for
466   Future Gene Activation. *Cell* 182, 127-144.e23 (2020).

467   36. Zhao, Q., Zoysa, R. S. S. de, Wang, D., Jayawardhana, D. A. & Guan, X. Real-Time Monitoring of
468   Peptide Cleavage Using a Nanopore Probe. *J Am Chem Soc* 131, 6324–6325 (2009).

469   37. Cao, C. *et al.* Single-molecule sensing of peptides and nucleic acids by engineered aerolysin
470   nanopores. *Nature Communications* 10, 4918 (2019).

471   38. Li, S. *et al.* T232K/K238Q Aerolysin Nanopore for Mapping Adjacent Phosphorylation Sites of a Single
472   Tau Peptide. *Small Methods* 4, 2000014 (2020).

473   39. Syganow, A. & Kitzing, E. von. (In)validity of the Constant Field and Constant Currents Assumptions in
474   Theories of Ion Transport. *Biophys J* 76, 768–781 (1999).

475   40. Isralewitz, B., Izrailev, S. & Schulten, K. Binding pathway of retinal to bacterio-opsin: a prediction by
476   molecular dynamics simulations. *Biophys J* 73, 2972–2979 (1997).

477   41. Grubmüller, H., Heymann, B. & Tavan, P. Ligand Binding: Molecular Mechanics Calculation of the
478   Streptavidin-Biotin Rupture Force. *Science* 271, 997–999 (1996).

479   42. Wilson, J., Sarthak, K., Si, W., Gao, L. & Aksimentiev, A. Rapid and Accurate Determination of
480   Nanopore Ionic Current Using a Steric Exclusion Model. *ACS Sensors* 4, 634–644 (2019).

481   43. Rathert, P., Dhayalan, A., Ma, H. & Jeltsch, A. Specificity of protein lysine methyltransferases and
482   methods for detection of lysine methylation of non-histone proteins. *Mol Biosyst* 4, 1186–1190 (2008).

483   44. Weirich, S., Khella, M. S. & Jeltsch, A. Structure, Activity and Function of the Suv39h1 and Suv39h2
484   Protein Lysine Methyltransferases. *Life* 11, 703 (2021).

485   45. Sigworth, F. J. & Klemic, K. G. Microchip Technology in Ion-Channel Research. *Ieee T Nanobiosci* 4,
486   121–127 (2005).

487   46. Klatt, J.-N. *et al.* Tryptic digestion of human serum for proteomic mass spectrometry automated by
488   centrifugal microfluidics. *Lab Chip* 20, 2937–2946 (2020).

489   47. Phillips, J. C. *et al.* Scalable molecular dynamics on CPU and GPU architectures with NAMD. *J Chem*
490   *Phys* 153, 044130 (2020).

491   48. MacKerell, A. D. *et al.* All-Atom Empirical Potential for Molecular Modeling and Dynamics Studies of
492   Proteins †. *J Phys Chem B* 102, 3586–3616 (1998).

493   49. Yoo, J. & Aksimentiev, A. New tricks for old dogs: improving the accuracy of biomolecular force fields
494   by pair-specific corrections to non-bonded interactions. *Phys Chem Chem Phys* 20, 8432–8449 (2018).

495   50. Miyamoto, S. & Kollman, P. A. Settle: An analytical version of the SHAKE and RATTLE algorithm for
496   rigid water models. *J Comput Chem* 13, 952–962 (1992).

497   51. Andersen, H. C. Rattle: A "velocity" version of the shake algorithm for molecular dynamics
498   calculations. *J Comput Phys* 52, 24–34 (1983).

499   52. Darden, T., York, D. & Pedersen, L. Particle mesh Ewald: An N ·log(N) method for Ewald sums in
500   large systems. *J Chem Phys* 98, 10089–10092 (1993).

501   53. Martyna, G. J., Tobias, D. J. & Klein, M. L. Constant pressure molecular dynamics algorithms. *J Chem*
502   *Phys* 101, 4177–4189 (1994).

503   54. Humphrey, W., Dalke, A. & Schulten, K. VMD: Visual molecular dynamics. *J Mol Graphics* 14, 33–38
504   (1996).

505   55. Aksimentiev, A. & Schulten, K. Imaging α-Hemolysin with Molecular Dynamics: Ionic Conductance,
506   Osmotic Permeability, and the Electrostatic Potential Map. *Biophys J* 88, 3745–3761 (2005).

507   56. Lucas, F. L. R. *et al.* The Manipulation of the Internal Hydrophobicity of FraC Nanopores Augments
508   Peptide Capture and Recognition. *ACS Nano* 15, 9600–9613 (2021).

509

510

511 **Extended Data Figures:**

g	peptides	τ /ms from dwell-time fit	τ /ms from ln(dwell-time) fit
	R_7L (wt)	22.72	22.40
	R_7L (R220S)	41.79	38.90
	R_7I (wt)	22.32	23.00
	R_7I (R220S)	39.90	38.91

512

513 *Extended Data Fig. 1| Dwell-time prologation due to R220 single point mutagenesis. a-d, Prolongation of dwell-times of hepta-*
514 *arginine-leucin, R_7L, and hepta-arginine-isoleucin, R_7I, peptides in the R220S mutant (blue) vs. wt-AeL pore (black). e, f, enhanced*
515 *discrimination of the isomeric peptides using the R220S mutant.*

516

19
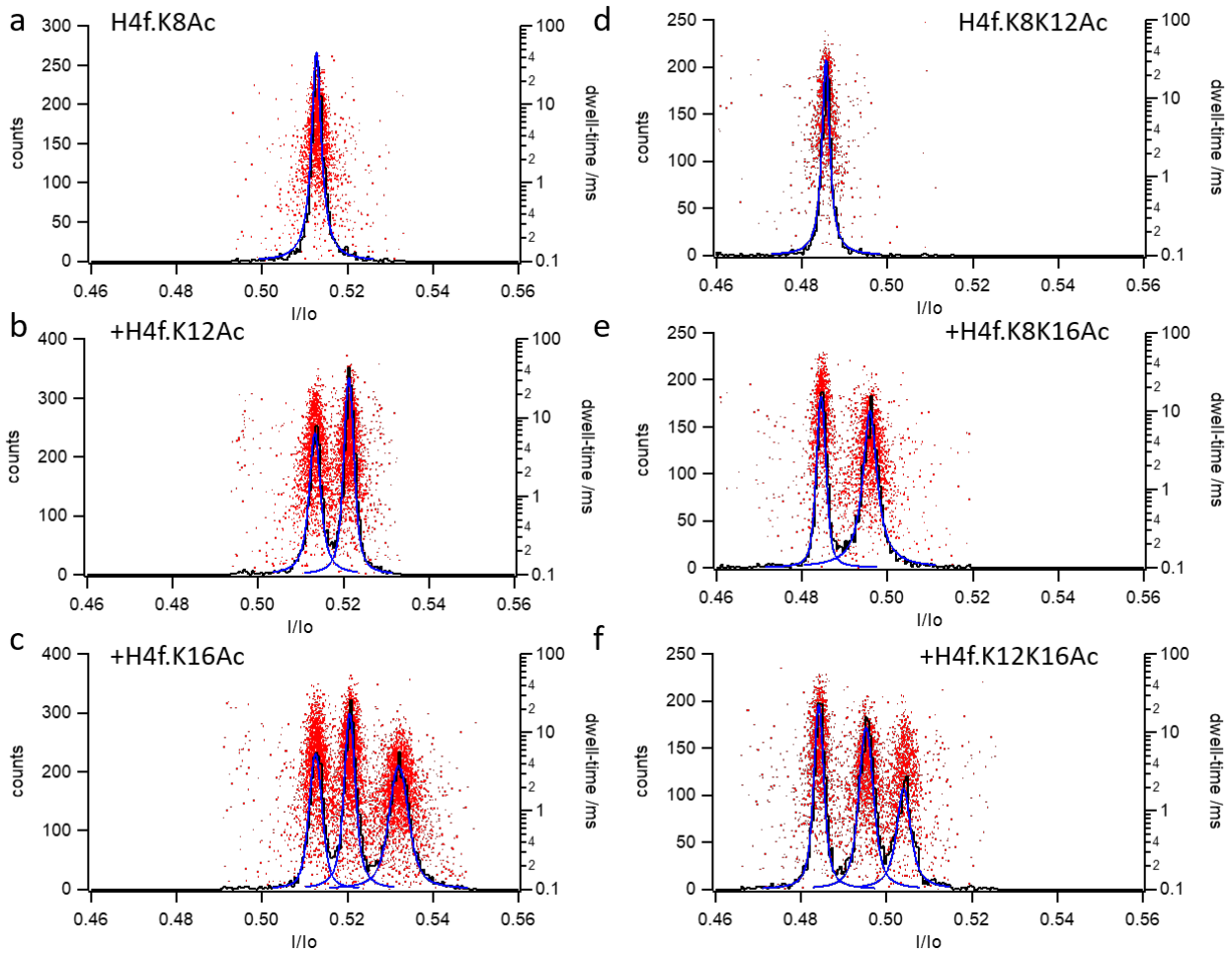
517

518   ***Extended Data Fig. 2|*** *Assignment of maxima for acetylated species of Hf4. by sequential addition of H4f. peptides with one (**a-c**)*
519   *or two (**d-f**) acetylated residues using sequential addition with the R220S mutant pore.*

520

521
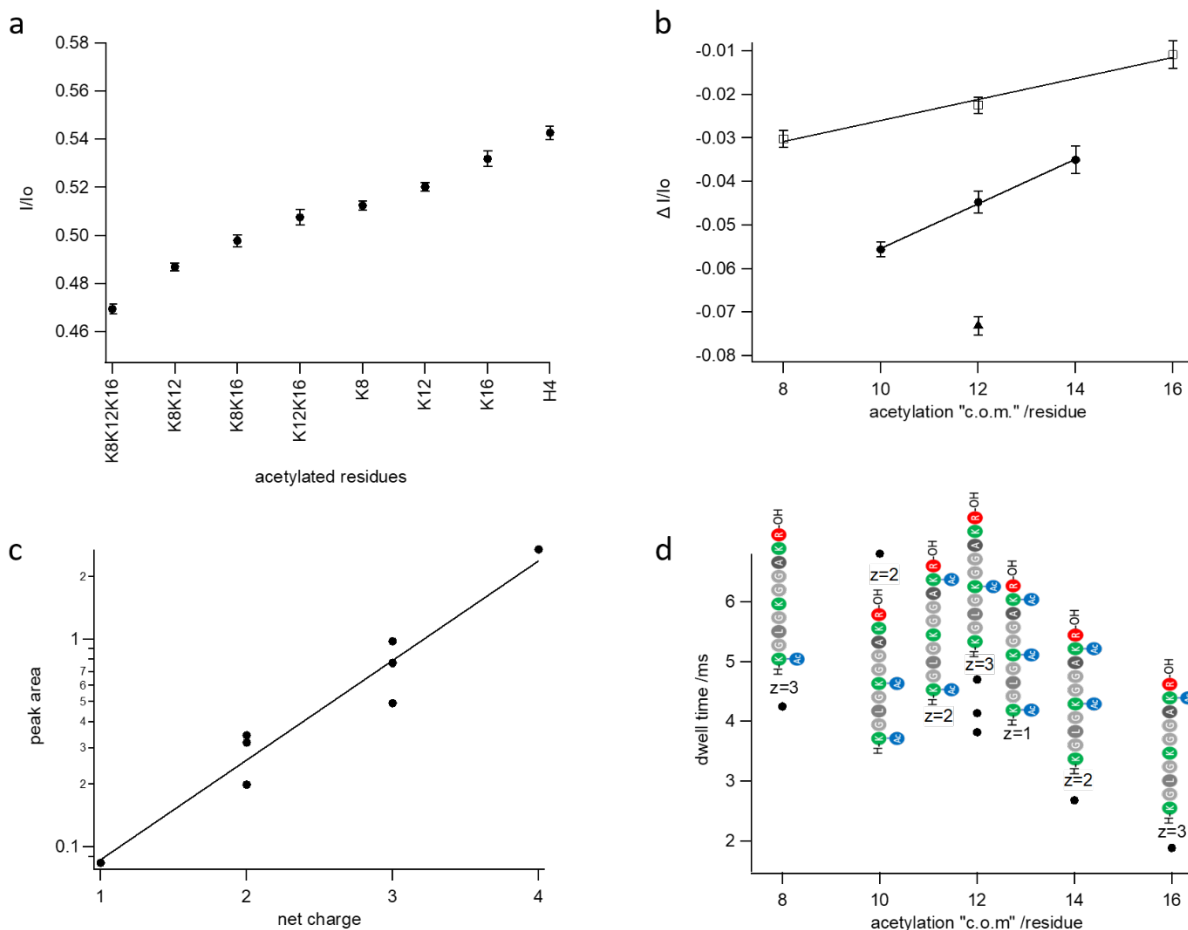
Extended Data Fig. 3| a, *Positions of maxima for interaction of H4f., H4f.K8Ac, H4f.K12Ac, H4f.K16Ac, H4f.K8K12Ac, H4f.K8K16Ac, H4f.K12K16Ac and H4f.K8K12K16Ac determined with the R220S mutant. Error bars show full width at half maximum of Voigt fits (**Fig. 1**d).* ***b***, *Shift in I/Io produced by acetylation plotted against the mean position or „center of mass, c.o.m." of the modification for single (open squares), double (filled circles) and triple acetylation (filled triangles).* ***c***, *Logarithmic dependence of peak area as a measure of event frequency on net charge of the peptide. Note decrease of frequency with loss of net charge due to acetylation.* ***d***, *Characteristic dwell-times (see* **Extended Data Fig. 4***) vs. acetylation „center of mass". Note increase from single acetylation at position 16 to double acetylation at positions 8 and 12. Charge numbers are given to show the absence of dependence of dwell-time on peptide charge.*
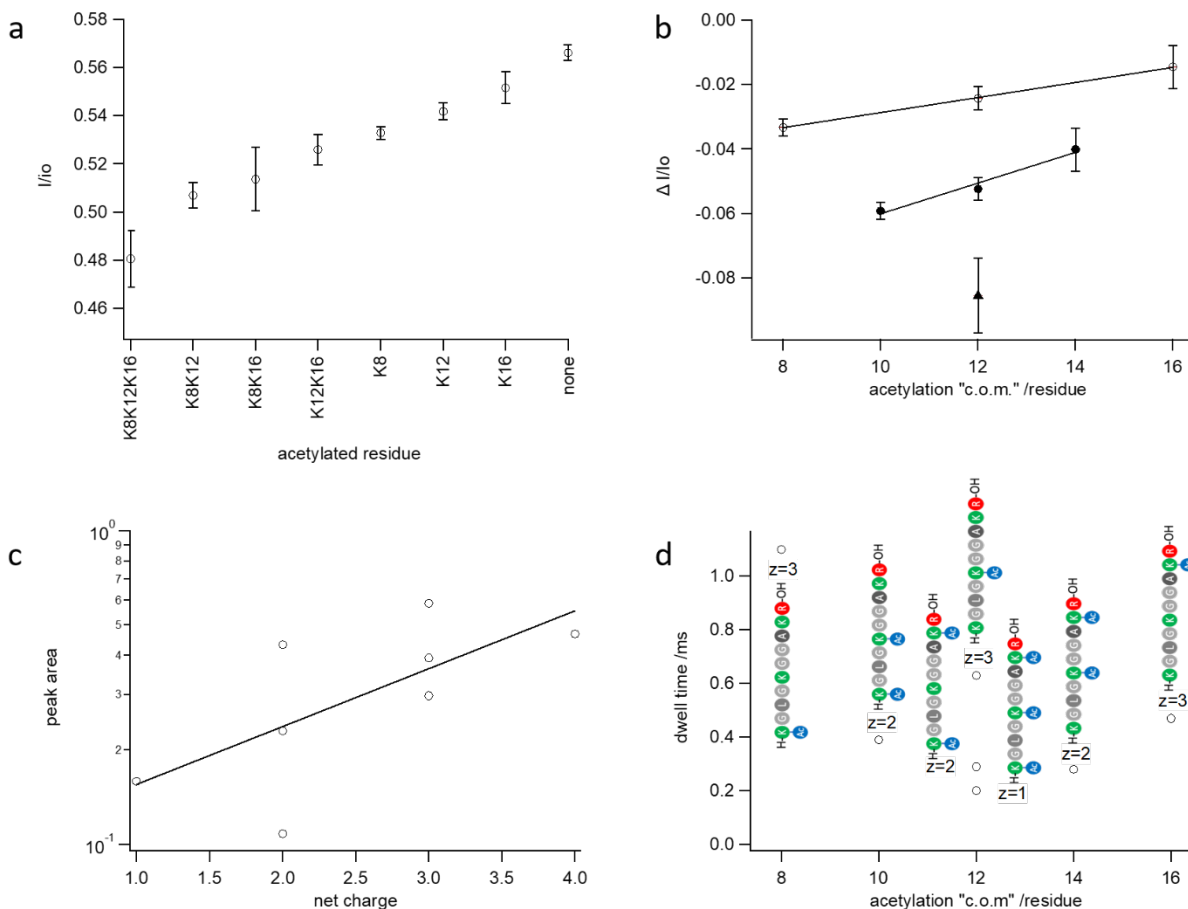
530

21
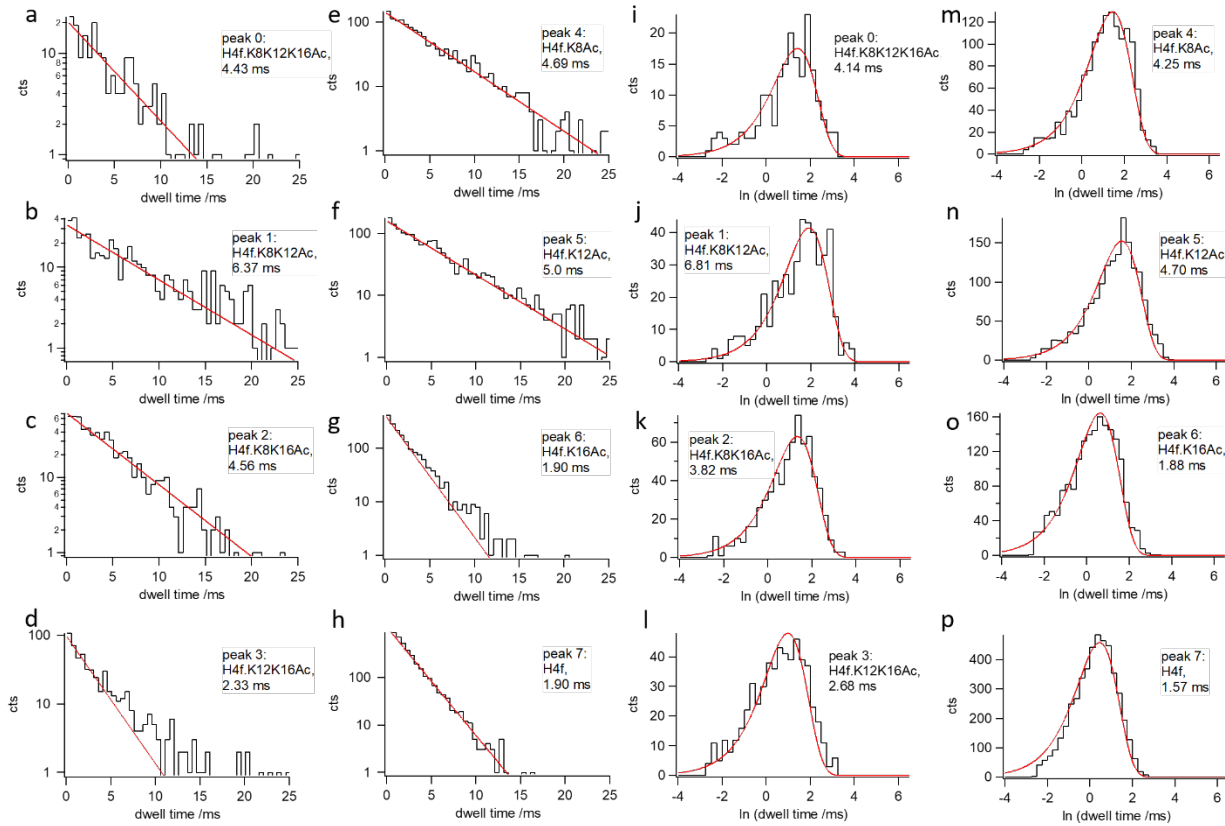
Extended Data Fig. 4| *Dwell-time distributions for interaction of H4f., H4f.K8Ac, H4f.K12Ac, H4f.K16Ac, H4f.K8K12Ac, H4f.K8K16Ac, H4f.K12K16Ac and H4f.K8K12K16Ac with the R220S mutant.* **a-h**, *semilogarithmic plots;* **i-p**, *histograms of natural logarithm of dwell-times. Red lines: monoexponential fits.*
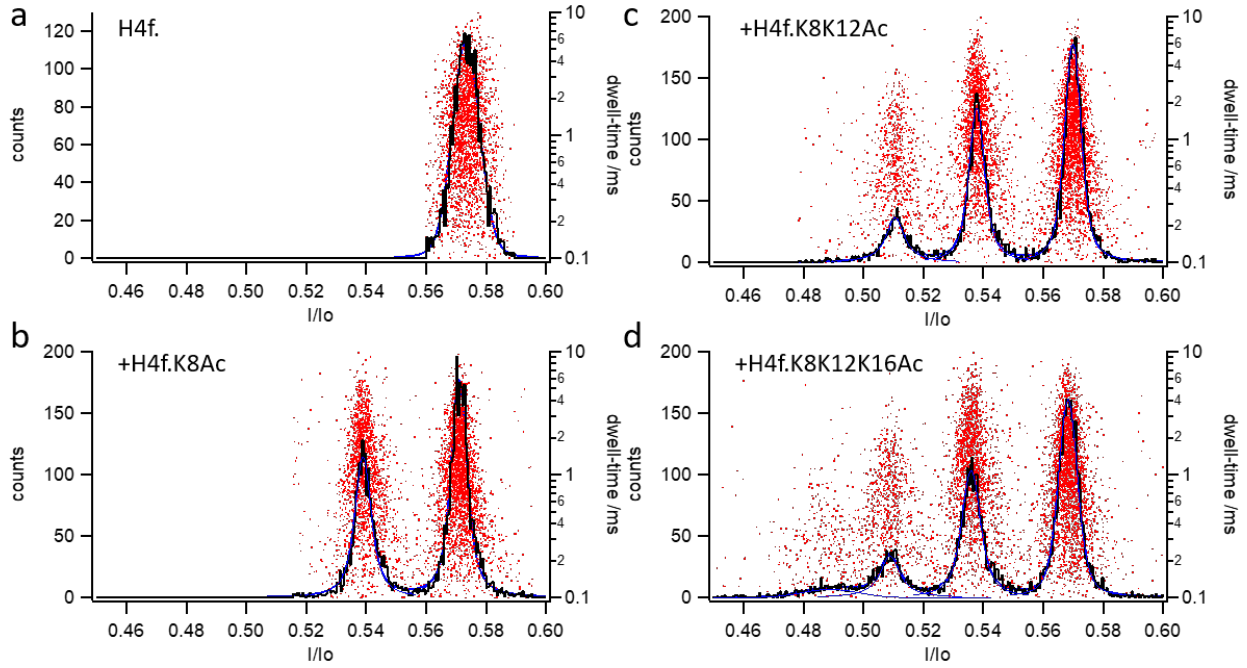
Extended Data Fig. 5| *Assignment of maxima to species H4f., H4f.K8Ac, H4f.K8K12Ac and H4f.K8K12K16Ac using sequential peptide addition with the wt-AeL pore.*

23

540
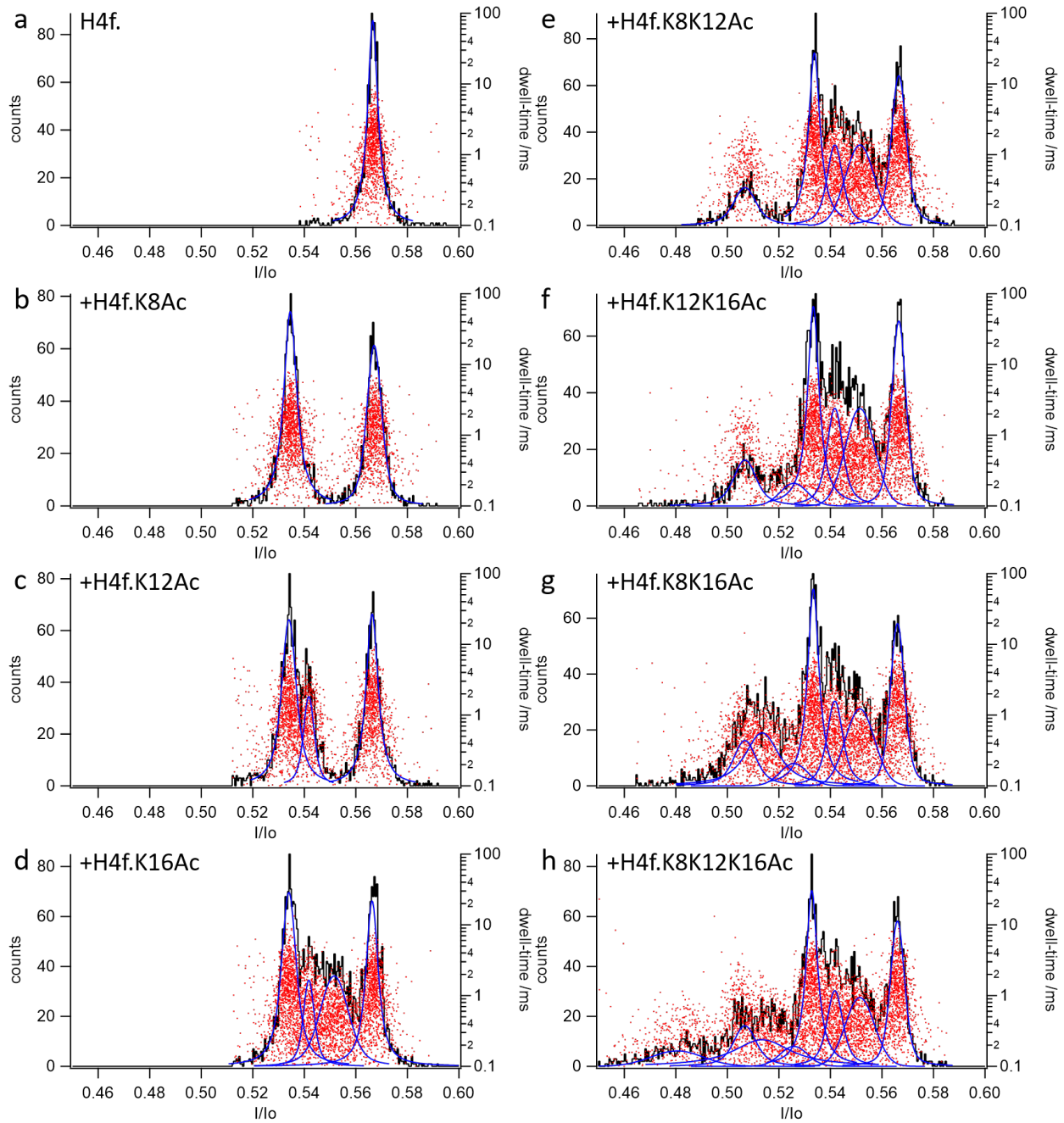
Extended Data Fig. 6| *Assignment of maxima to species H4f., H4f.K8Ac, H4f.K12Ac, H4f.K16Ac, H4f.K8K12Ac, H4f.K8K16Ac, H4f.K12K16Ac and H4f.K8K12K16Ac using sequential peptide addition with the wt-AeL pore.*

543

544
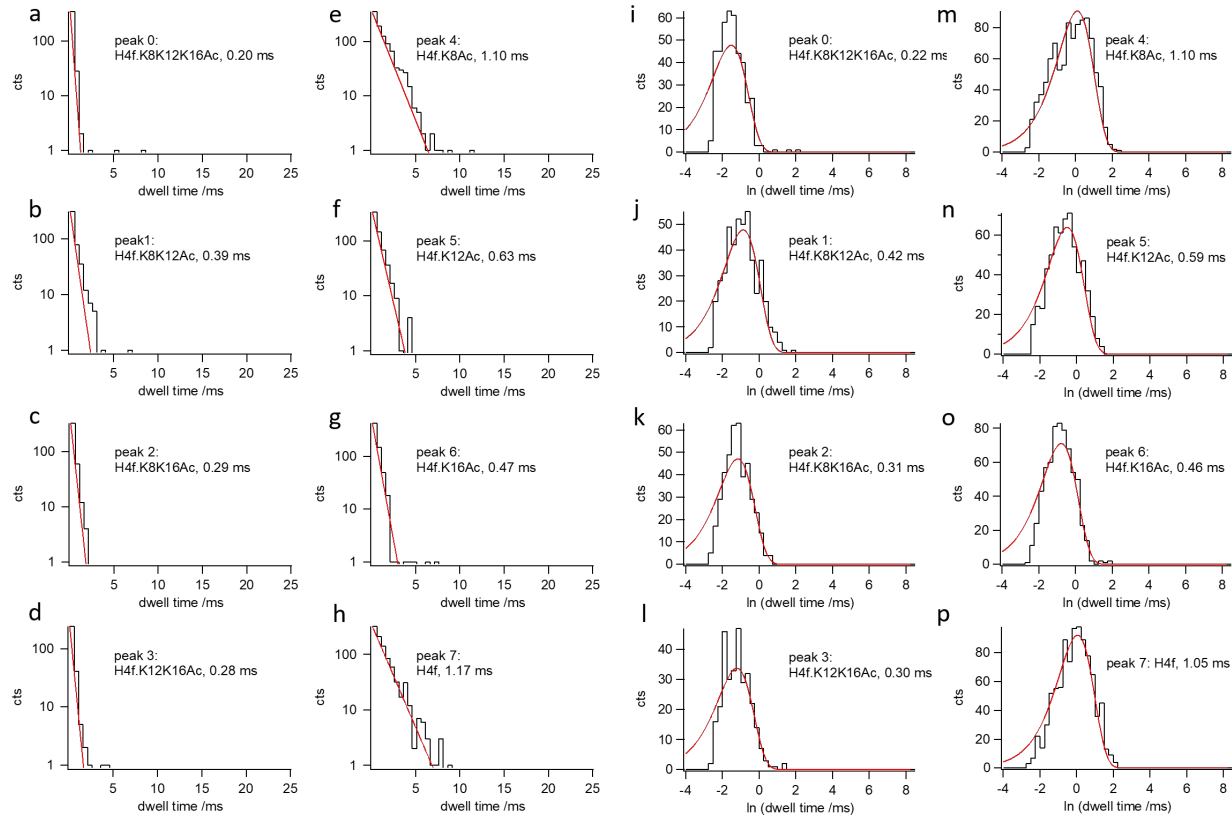
Extended Data Fig. 7| *Dwell-time distributions for interaction of H4f., H4f.K8Ac, H4f.K12Ac, H4f.K16Ac, H4f.K8K12Ac, H4f.K8K16Ac, H4f.K12K16Ac and H4f.K8K12K16Ac with the wt-AeL pore.* **a-h,** *Semilogarithmic plots.* **i-p,** *Histograms of natural logarithm of dwell-times. Red lines: monoexponential fits.*

548

Extended Data Fig. 8| a, Positions of maxima for interaction of H4f., H4f.K8Ac, H4f.K12Ac, H4f.K16Ac, H4f.K8K12Ac, H4f.K8K16Ac, H4f.K12K16Ac and H4f.K8K12K16Ac with the wt-AeL pore. Error bars show full width at half maximum of Voigt fits (**Fig. 1**). **b,** Shift in I/Io produced by acetylation plotted against the mean position or „center of mass, c.o.m." of the modification for single (open squares), double (filled circles), and triple acetylation (filled triangles). **c,** Logarithmic dependence of peak area as a measure of event frequency on net charge of the peptide. Note decrease of frequency with loss of net charge due to acetylation. **d,** Characteristic dwell-times (see **Extended Data Fig. 4**) vs. acetylation „center of mass". Note decrease from single acetylation at position 8, 12 or 16 to double acetylation at positions 8 and 12 or 8 and 16. Charge numbers are given to show the absence of dependence of dwell-time on peptide charge.
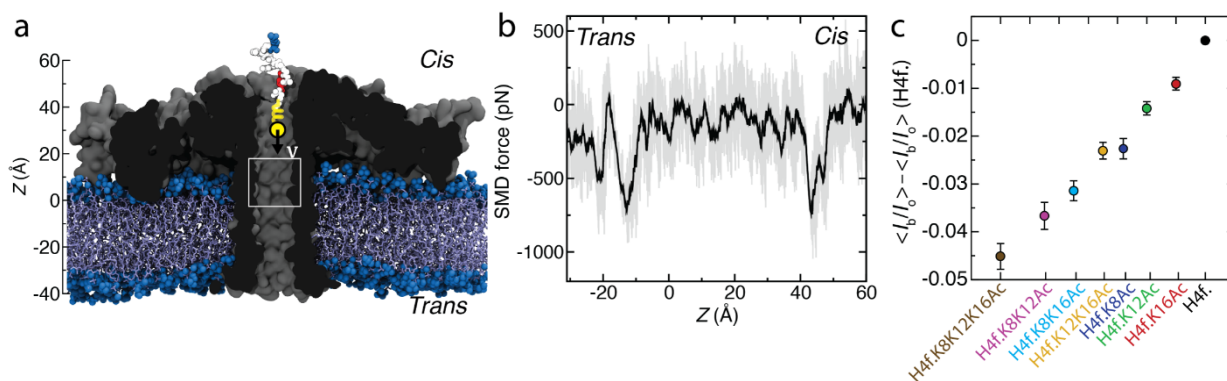
Extended Data Fig. 9| Steered MD simulation of H4f.K8Ac peptide through R220S aerolysin. a, initial state of a 100 ns steered molecular dynamics simulation (same as in **Fig. 2a**) where an H4f.K8Ac peptide (vdw spheres) is pulled by a harmonic spring with
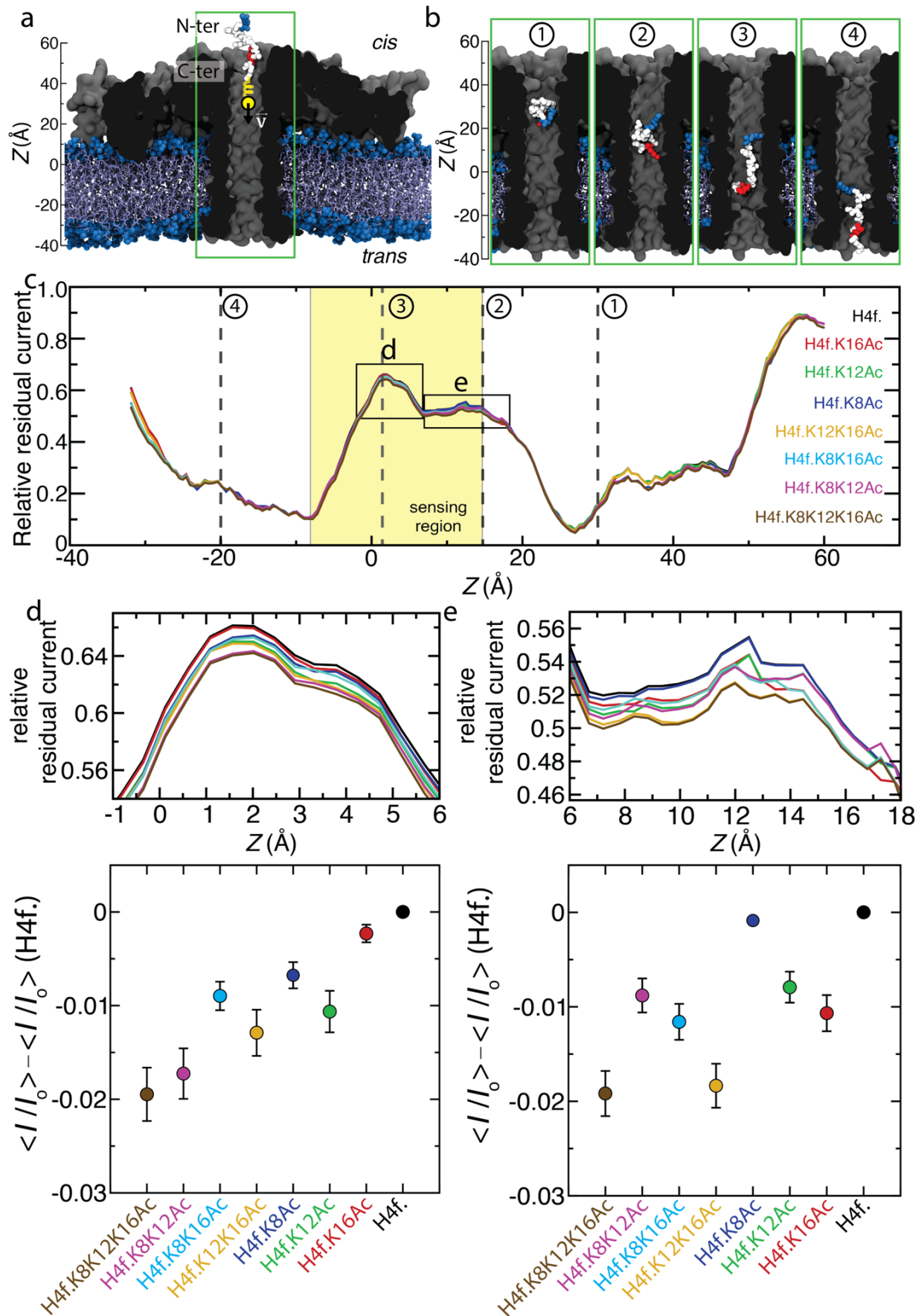
562   *a constant velocity of 1 Å/ns through an aerolysin nanopore (cutaway molecular surface), embedded in a lipid membrane (blue)*
563   *and submerged in 2 M KCl electrolyte (not shown). The C-terminus of the peptide is oriented towards the trans-side of the*
564   *membrane. The white rectangle indicates the region (-2 Å < z < 18 Å) used for averaging in panel c.* **b,** *Force exerted by the SMD*
565   *spring (running average: 0.5 Å) vs. the z coordinate of the H4f.K8Ac peptide;* **c,** *Simulated average relative currents produced by*
566   *the acetylated peptides calculated as a difference from the baseline H4f. peptide within the region highlighted in the inset of* **Fig.**
567   **2b** *(-2 Å < z < 18 Å). The error bars show the standard error calculated using 80 current values*

568
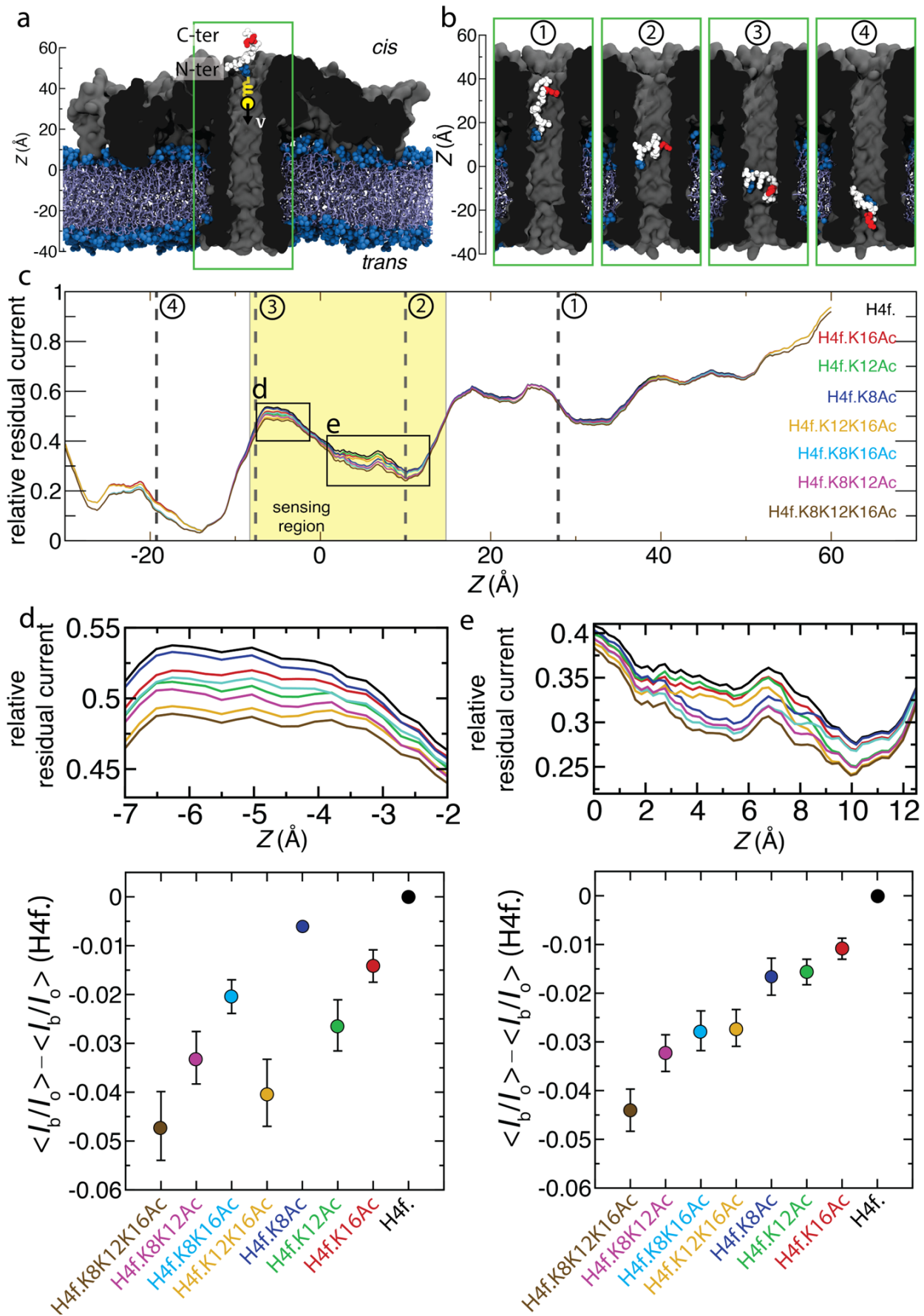
570 ***Extended Data Fig. 10| Blockade current of acetylation modification depends on the global conformation of the peptide in the***
571 ***nanopore. a**, initial state of a 100 ns steered MD simulation where an H4f.K8Ac peptide (vdW spheres) is pulled by a harmonic*
572 *spring with a constant velocity of 1 Å/ns through an aerolysin nanopore (cutaway molecular surface), embedded in a lipid*
573 *membrane (blue) and submerged in 2 M KCl electrolyte (not shown). The N-terminus of the peptide is oriented towards the trans-*
574 *side of the membrane. The orientation is opposite to that shown in **Fig. 2**a. The green box shows the nanopore volume shown in*
575 *panel b. **b**, Representative conformations of the H4f.K8Ac peptide along the SMD simulation chronologically shown from left to*
576 *right. As the simulation progresses, the peptide reverses its orientation leading to the C-terminal end of the peptide facing the*
577 *trans-side of the pore while the peptide exits the pore. **c**, Relative residual current versus center of mass z coordinate of the*
578 *acetylated H4f. peptides. The coordinate axis is defined in panel a. The conformations from panel b are marked using vertical*
579 *dotted lines and numbered circles defined in panel b. The currents were computed using SEM [42] and were running-averaged with*
580 *a 5 Å window. The highlighted region shows the sensing volume (-9 Å < z < 15 Å) of the wt-AeL pore [23]. Two black boxes mark the*
581 *zoomed in region highlighted in panels d and e. **d**, Relative residual current versus center of mass z coordinate between z=-7 Å and*
582 *z=-2 Å as highlighted in c. The lower panel shows the average relative residual current and its standard error over the 21 data*
583 *points in the shown region. The ordering of the peptide currents depends on the peptide conformation. The peptides are arranged*
584 *in the x-axis in an increasing order according to their experimental blockade values. **e**, Same as panel d but for the region between*
585 *z=0 Å to z=12.5 Å (53 data points), highlighted in c.*

586

587

588 ***Extended Data Fig. 11| Blockade current of acetylation modification depends on the global conformation of the peptide in the***
589 ***nanopore. a,*** *Initial state of a 100 ns steered molecular dynamics simulation where an H4f.K8Ac peptide (vdW spheres) is pulled*
590 *using a harmonic spring with a constant velocity of 1 Å/ns through an aerolysin nanopore (cutaway molecular surface), embedded*
591 *in a lipid membrane (blue) and submerged in 2 M KCl electrolyte (not shown). The C-terminus of the peptide is oriented towards*
592 *the trans-side of the membrane. The global orientation of the peptide is the same as that in the trajectory shown in* ***Fig. 2****a, but*
593 *the simulation stars from a slightly different microscopic configuration. The green box shows the nanopore volume shown in panel*
594 *b.* ***b,*** *Representative conformations of the H4f.K8Ac peptide along the SMD simulation chronologically shown from left to right.* ***c,***
595 *Relative residual current versus center of mass z coordinate of the acetylated H4f. peptides. The coordinate axis is defined in panel*
596 *a. The conformations from panel b are marked using vertical dotted lines and numbered circles defined in panel b. The currents*
597 *were computed using SEM [42] and were running-averaged with a 5 Å window. The highlighted region shows the sensing volume (-*
598 *9 Å < z < 15 Å) of the wt-AeL pore [23]. Two black boxes mark the zoomed in region highlighted in panels d and e.* ***d,*** *Relative residual*
599 *current versus center of mass z coordinate between z=-1 Å and z=6 Å as highlighted in c. The lower panel shows the average relative*
600 *residual current and its standard error over the 15 data points in the shown region. The ordering of the peptide currents depends*
601 *on the peptide conformation. The peptides are arranged in the x-axis in an increasing order according to their experimental*
602 *blockade values.* ***e,*** *Same as panel d but for the region between z=6 Å to z=18 Å (24 data points), highlighted in c.*

603
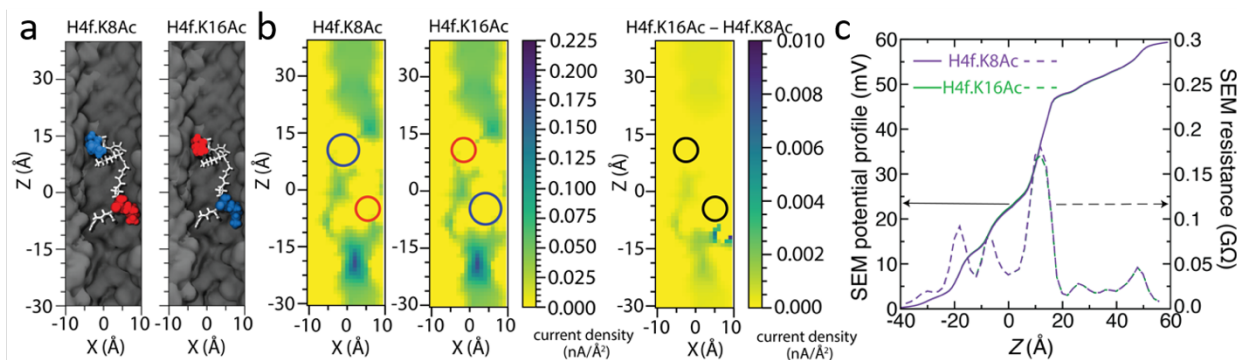
604

605 ***Extended Data Fig. 12| SEM analysis of H4f.K8Ac vs. H4f.K16Ac for another conformation of the H4f. peptide taken from the***
606 ***same SMD trajectory as that shown in Fig 2 of the main text. a,*** *Representative conformation (z height of 5 Å) of a H4f.K8Ac*
607 *peptide in the sensing region of the nanopore and the corresponding computational model of the H4f.K16Ac peptide. The peptide*
608 *residues are drawn as white sticks except the K8 and K16 residues which are shown as vdW spheres colored according to their*
609 *acetylation state: acetylated (blue) and unmodified (red).* ***b,*** *Local density of transmembrane ion current (its z component) near*
610 *the H4f.K8Ac (left) and H4f.K16Ac (center) peptides and their difference (right). The currents were computed using SEM over a 1 Å*
611 *grid. The heat map shows a cross section of the nanopore volume along the pore axis. The circles indicate the approximate locations*
612 *of the K8 and K16 residues.* ***c,*** *Electrostatic potential along the nanopore axis for the H4f.K8Ac (purple) and H4f.K16Ac (green)*
613 *peptide systems (solid lines, left axis) and local resistance of the nanopore volume (dashed lines, right axis). The local resistance*
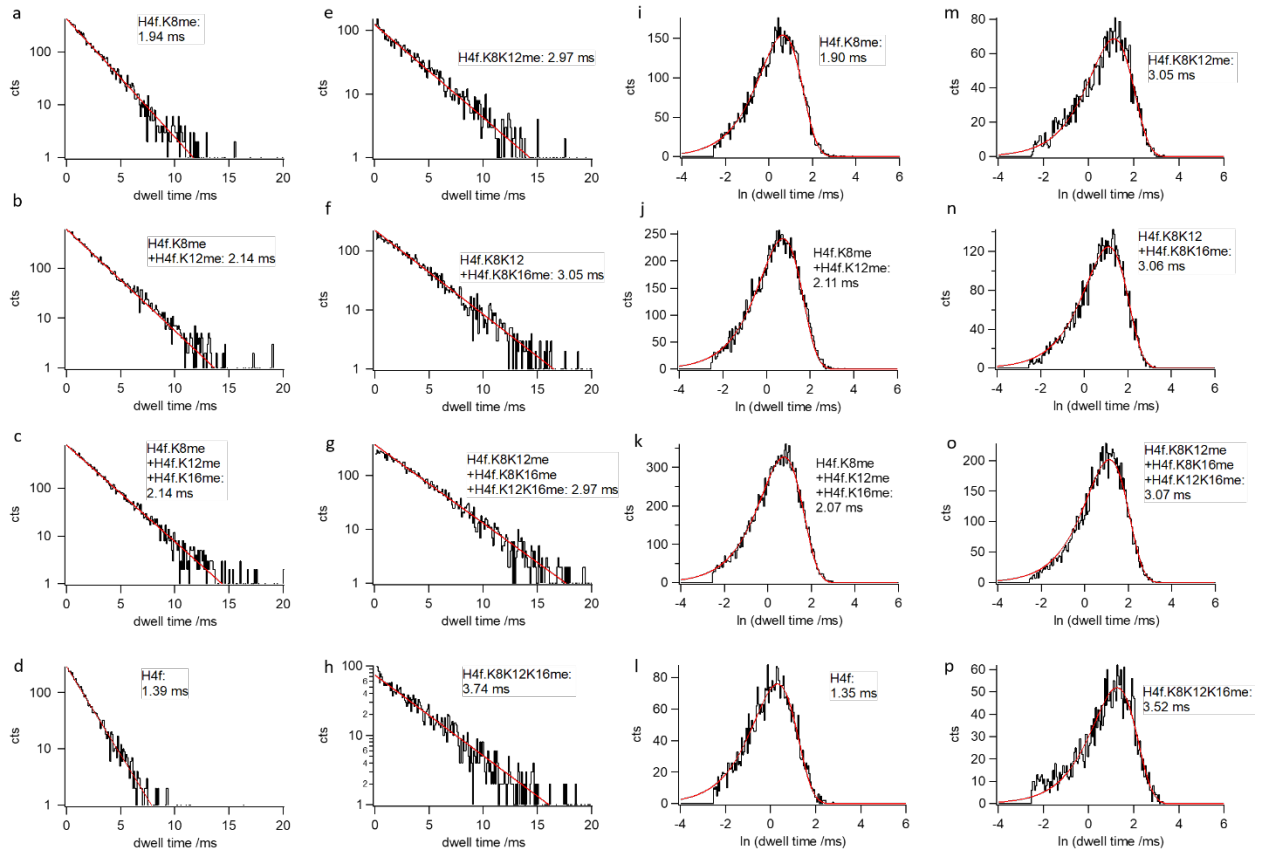614 *was computed from the local electrostatic potential using 4 Å segments.*

615

616
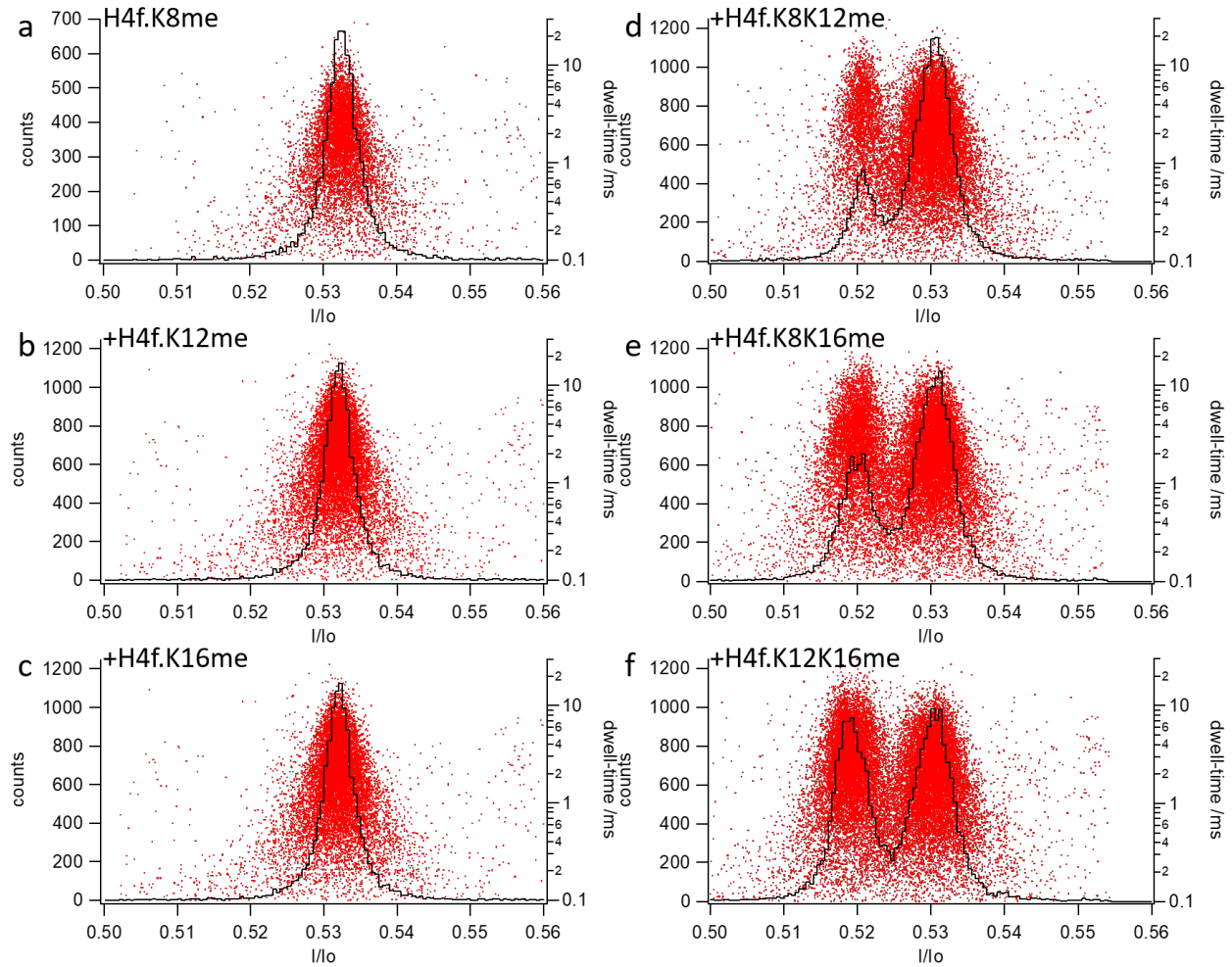
Extended Data Fig. 13| *Assignment of maxima for singly and doubly monomethylated peptoforms of H4f. using sequnetianl*
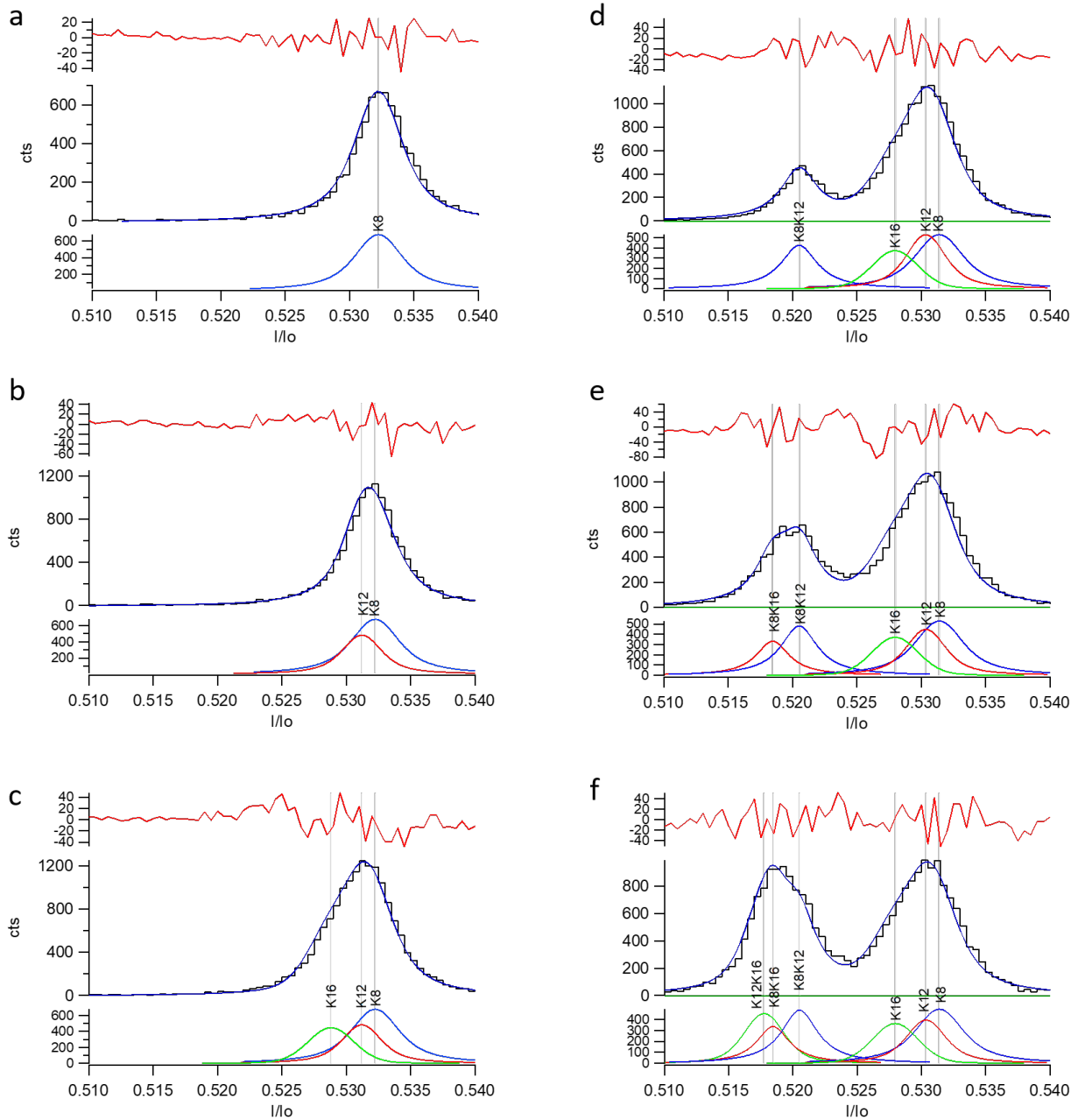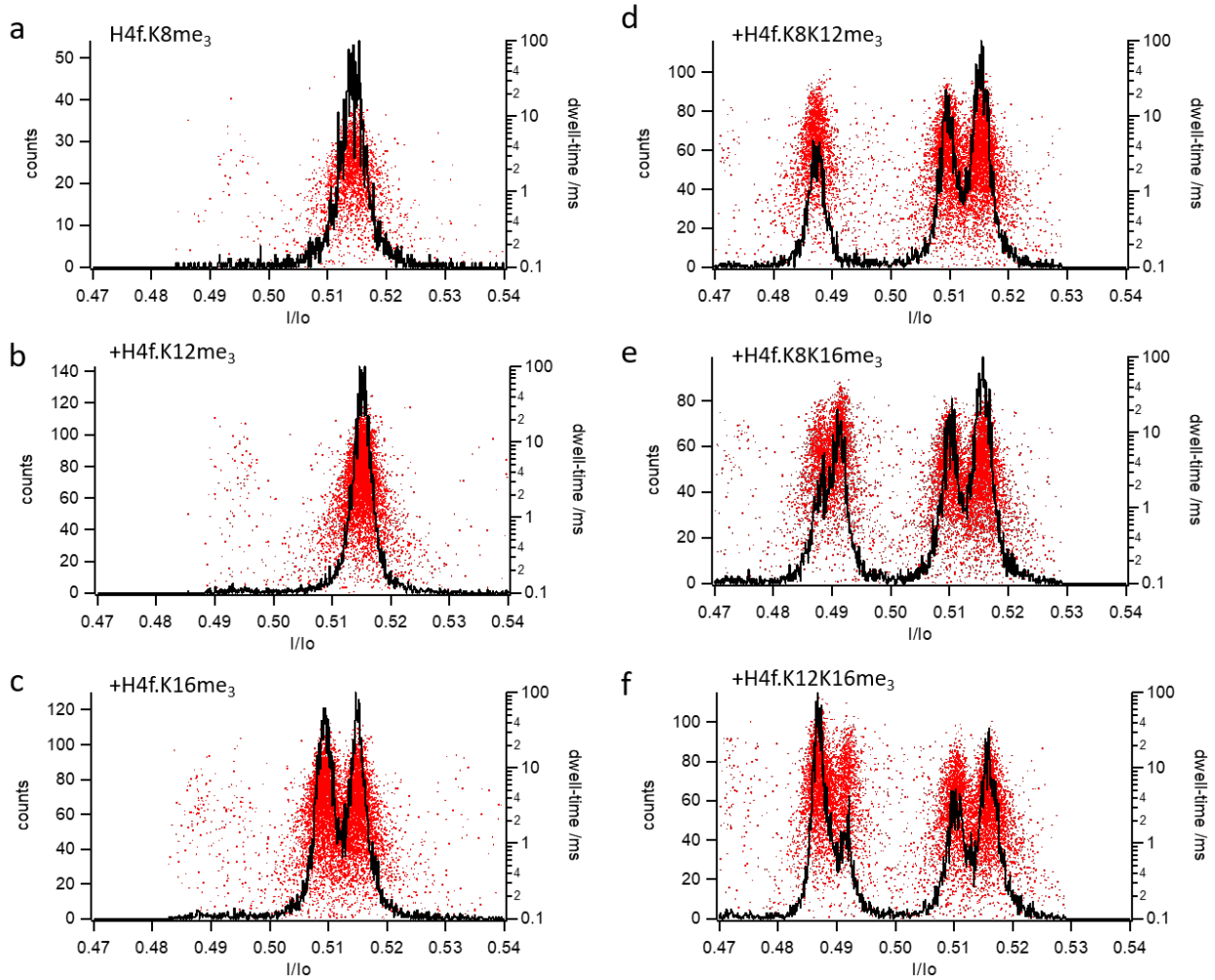617
618 *addition with the R220S mutant.*

619

Extended Data Fig. 14| *Dwell-time distributions for the interaction of singly, doubly and triply monomethylated peptoforms of H4f with the R220S mutant.*

624

Extended Data Fig. 15|: *discrimination of singly (**a-c**) and doubly (**d-f**) monomethylated isomeric H4f. peptoforms using sequential addition with the R2020S mutant.*

627

628

629 **Extended Data Fig. 16|** *Assignment of maxima for singly and doubly trimethylated peptoforms of H4f. using sequential addition*
630 *with the R220S mutant.*

631 <

632

633 **Extended Data Fig. 17|** *Dwell-time distributions for the interaction of singly, doubly and triply trimethylated peptoforms of H4f.*
634 *with the R220S mutant.*

635
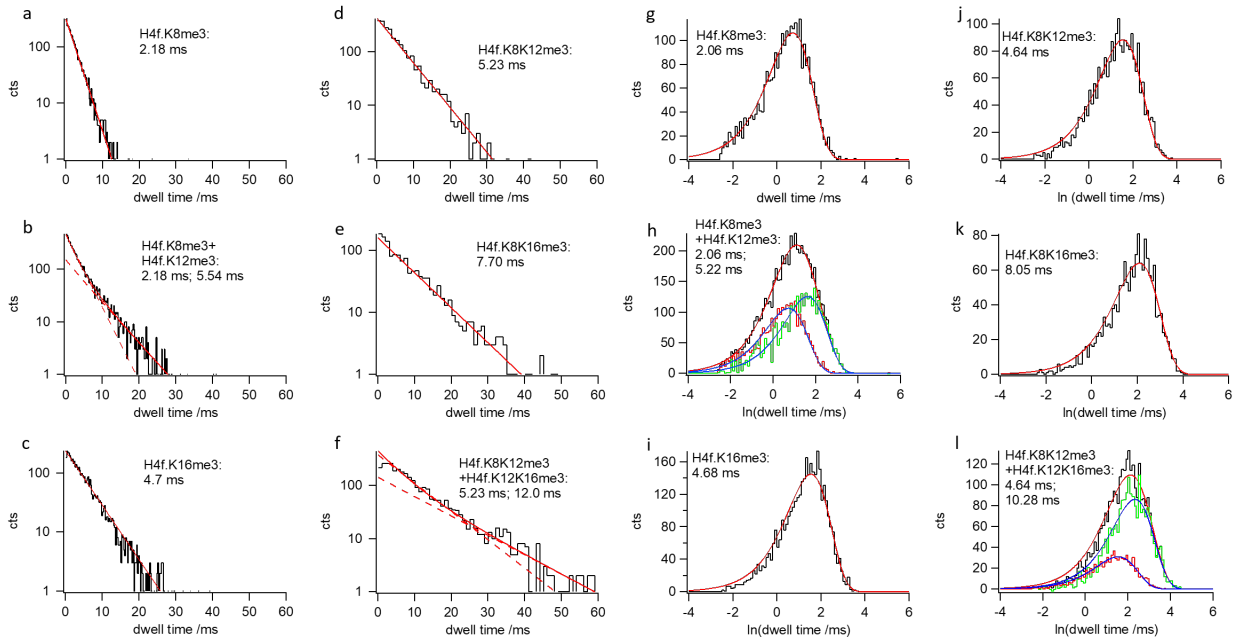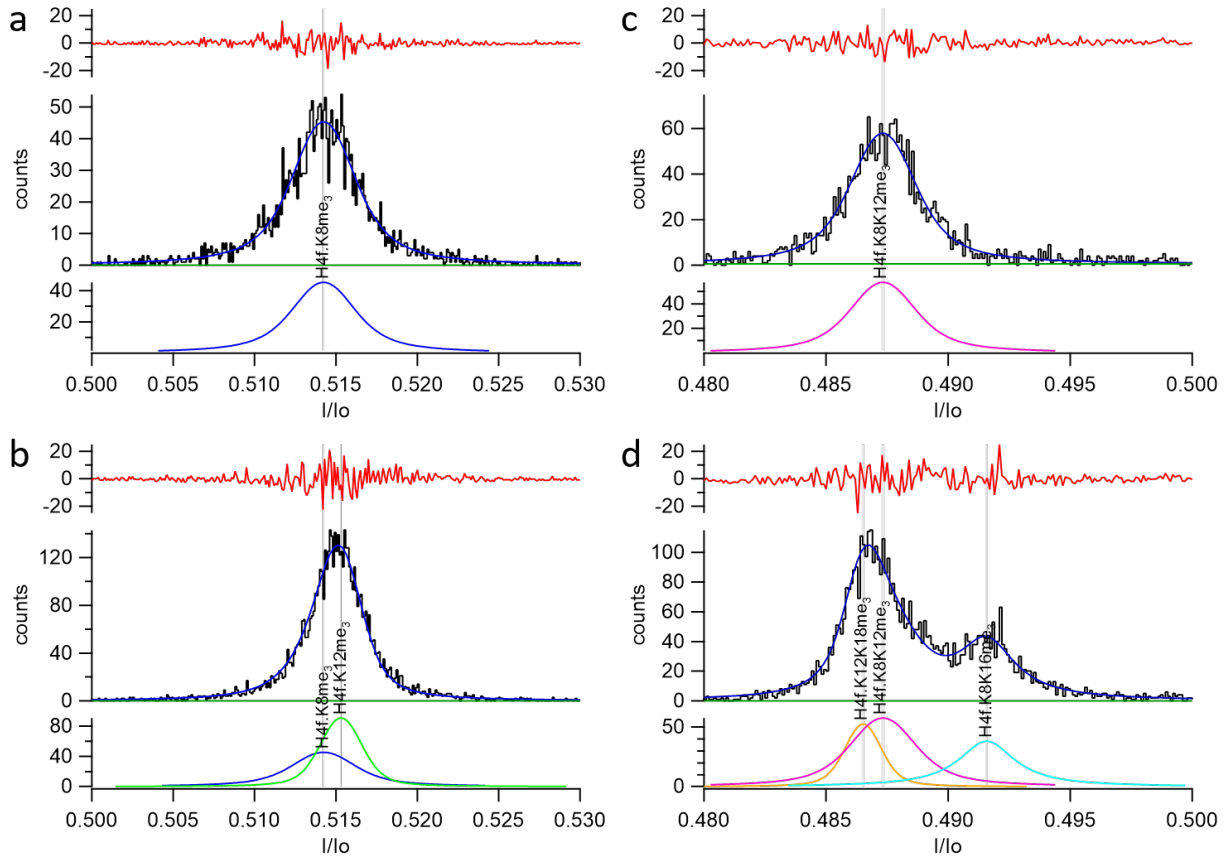
636

637 **Extended Data Fig. 18|** *Discrimination of singly (**a-c**) and doubly (**d-f**) trimethylated isomeric H4f. peptoforms with the R220S*
638 *mutant.*

639

WT:

$$Ac: \genfrac{}{}{0pt}{}{K8}{\genfrac{}{}{0pt}{}{K12}{K16}} < \genfrac{}{}{0pt}{}{K8}{K12} < \genfrac{}{}{0pt}{}{K8}{K16} < \genfrac{}{}{0pt}{}{K12}{K16} < K8 < K12 < K16 \ll H4f$$

R220S:

$$Ac: \genfrac{}{}{0pt}{}{K8}{\genfrac{}{}{0pt}{}{K12}{K16}} \ll \genfrac{}{}{0pt}{}{K8}{K12} \ll \genfrac{}{}{0pt}{}{K8}{K16} \ll \genfrac{}{}{0pt}{}{K12}{K16} \ll K8 \ll K12 \ll K16 \ll H4f$$

$$me: \genfrac{}{}{0pt}{}{K8}{\genfrac{}{}{0pt}{}{K12}{K16}} \ll \genfrac{}{}{0pt}{}{K12}{K16} < \genfrac{}{}{0pt}{}{K8}{K16} < \genfrac{}{}{0pt}{}{K8}{K12} \ll K16 < K12 < K8 \ll H4f$$

$$me_3: \genfrac{}{}{0pt}{}{K8}{\genfrac{}{}{0pt}{}{K12}{K16}} \ll \genfrac{}{}{0pt}{}{K12}{K16} < \genfrac{}{}{0pt}{}{K8}{K12} \ll \genfrac{}{}{0pt}{}{K8}{K16} \ll K16 \ll K8 < K12 \ll H4f$$

640

641 ***Extended Data Fig. 19|Overview of the sequences of depth of block (I/Io) observed in this study.***

642
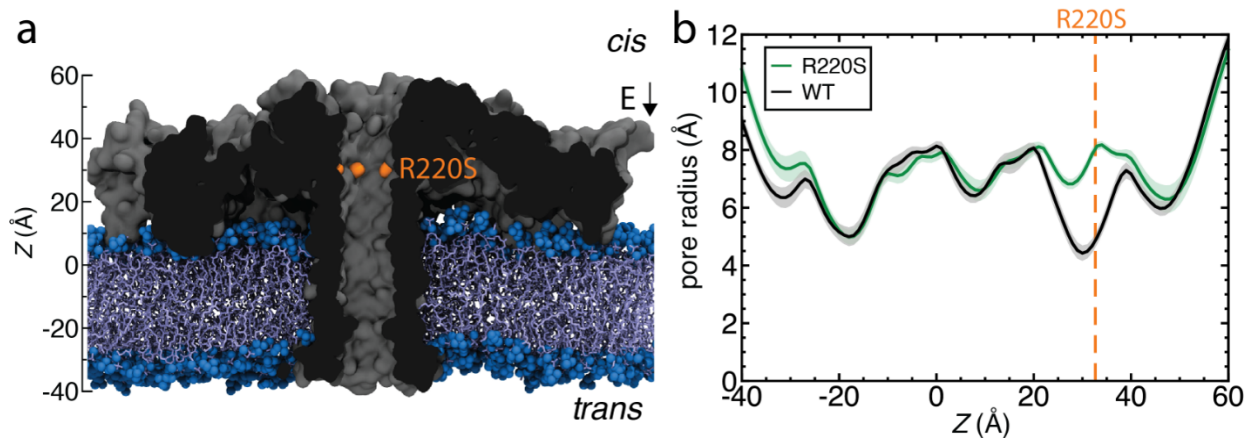
643

644 ***Extended Data Fig. 20| Structure of R220S mutant aerolysin. a,*** *Initial state of an MD simulation where a R220S aerolysin*
645 *nanopore (cutaway molecular surface) is embedded in a lipid membrane (blue), submerged in 2 M KCl electrolyte (not shown) and*
646 *simulated under an applied electric field corresponding to a transmembrane voltage bias of -60 mV, as used experimentally in this*
647 *study Residue R220 is shown in orange.* ***b,*** *Pore radius of the R220S pore (green) and the wt-AeL pore (black)* [23] *is plotted along the*
648 *symmetry axis of the pore. The radius is calculated by using the HOLE software and averaged over the last 20 ns of the MD*
649 *simulation trajectory for R220S and wt-AeL nanopore.*

650
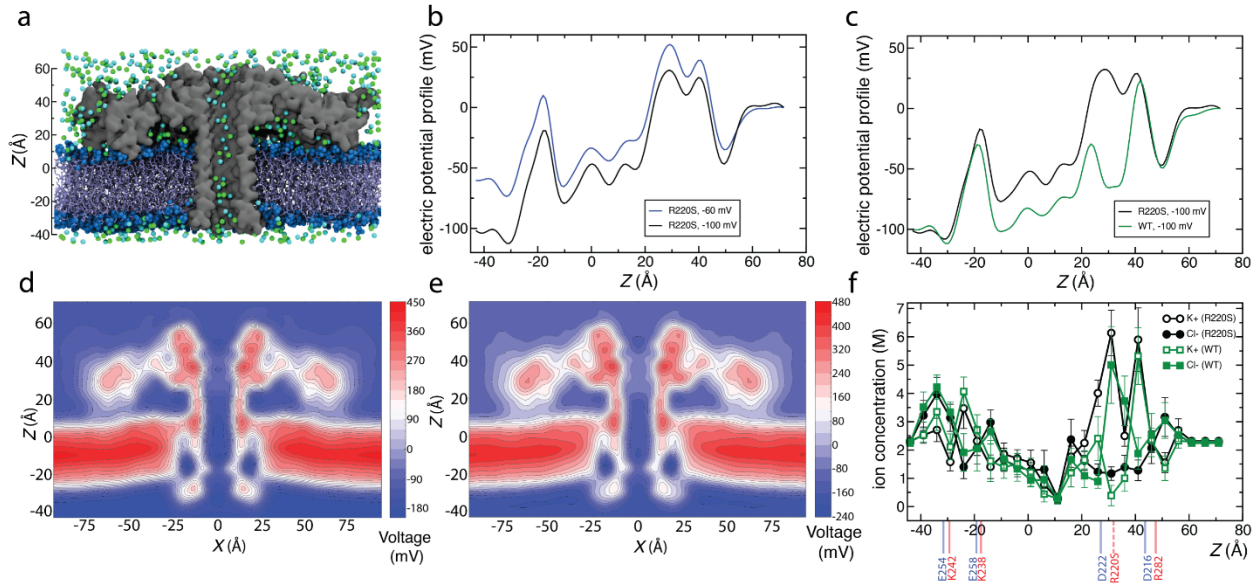
__Extended Data Fig. 21| Ion transport driven by electric field through R220S and wt-AeL nanopore. a__, Initial state of an MD simulation where a R220S aerolysin nanopore (gray cutaway molecular surface) is embedded in a lipid membrane (blue), submerged in 2 M KCl electrolyte (potassium and chloride shown as cyan and green spheres respectively) and simulated under an applied electric field corresponding to a transmembrane voltage bias of -60 mV, as used experimentally in this study. __b__, average electrostatic potential along the symmetry axis of R220S aerolysin (the z axis) at −60 mV (blue) and −100 mV (black). The plot was obtained by taking the average of instantaneous values of electrostatic potential along the symmetry axis over a 70 ns (R220S) and a 90 ns (wt) MD trajectory; __c:__ average electrostatic potential along the symmetry axis of R220S aerolysin (the z axis) at −100 mV (black) and wt-AeL at −100 mV and 2 M KCl electrolyte (green). The plot of R220S and wt-AeL was obtained by taking the average of instantaneous values of electrostatic potential along the symmetry axis over a 70 ns and 90 ns MD trajectory respectively. The average MD current is -0.13 nA at -100 mV for the wt-AeL pore and -0.21 nA at -100 mV for the R220S aerolysin pore. __d, e__, Two-dimensional electrostatic potential map of R220S aerolysin at −60 mV (d) and −100 mV (e) transmembrane bias. The map was obtained by averaging instantaneous distributions of electrostatic potentials over a 70 ns (R220S) and 90 ns (wt) MD trajectory and the sixfold symmetry of the channel. __f__, profiles of potassium (black, open circles) and chloride (black, filled circles) ion concentration along the symmetry axis of the R220S aerolysin nanopore. Also shown are the profiles of potassium (green, open squares) and chloride (green, filled squares) ion concentration along the symmetry axis of the wt-AeL nanopore. The ion concentration values are averaged over 5 Å z bins inside the pore (defined by the radius profile shown in __Extended Data Fig. 20__b) every 0.25 ns and further block averaged over 10 ns intervals in a total simulation time of 70 and 90 ns for the R220S and wt-AeL nanopore respectively. The ion concentration for z values outside the protein are calculated by counting the potassium and chloride ions in water molecules outside the protein that constitute the bulk water in the simulation system. Background blue and red lines represent positive and negative amino acid residues along the inner surface of the aerolysin pore, which are annotated by the amino acid type and residue number at the bottom. The dashed blue line represents the R220 positive amino acid that is mutated to a neutral serine in the R220S aerolysin pore.

673